
ENERGY-BASED COARSE-GRAINING IN MOLECULAR DYNAMICS: A FLOW-BASED FRAMEWORK WITHOUT DATA

A PREPRINT

 **Maximilian Stupp***

Professorship of Data-driven Materials Modeling
School of Engineering and Design
Technical University of Munich
maximilian.stupp@tum.de

 **P. S. Koutsourelakis***

Professorship of Data-driven Materials Modeling
School of Engineering and Design
Munich Data Science Institute (MDSI - Core Member)
Technical University of Munich
p.s.koutsourelakis@tum.de

ABSTRACT

Coarse-grained (CG) models provide an effective route to reducing the complexity of molecular simulations, but conventional approaches depend heavily on long all-atom molecular dynamics trajectories to adequately sample configurational space. This data dependence limits accuracy and generalizability, as unvisited configurations remain excluded from the resulting CG models.

We introduce a fully data-free, generative framework for coarse-graining that directly targets the all-atom Boltzmann distribution. The model defines a structured latent space comprising *slow* collective variables, associated with multimodal marginal densities capturing metastable states, and *fast* variables, represented through simple, unimodal conditional distributions. A learnable, bijective map from latent space to atomistic coordinates enables the automatic and accurate reconstruction of molecular structures. Training relies solely on the interatomic potential and minimizes the reverse Kullback–Leibler (KL) divergence via an energy-based objective. To stabilize optimization and ensure mode coverage, we employ an adaptive tempering scheme that promotes the exploration of diverse configurations. Once trained, the model can generate independent, one-shot equilibrium samples at full atomic resolution.

Validation on two synthetic systems, a double-well potential and a Gaussian mixture model, as well as on the benchmark alanine dipeptide, demonstrates that the method captures all relevant modes of the Boltzmann distribution, reconstructs atomic configurations with high fidelity, and automatically learns physically meaningful CG representations. These results suggest that the proposed framework provides a promising, data-free alternative to traditional CG techniques, offering both a principled approach to addressing the long-standing “chicken-and-egg” challenge in coarse-graining and an effective solution to the back-mapping problem by enabling accurate reconstruction of all-atom configurations.

Keywords Coarse-graining · Boltzmann distribution · Energy training · Normalizing Flow · Tempering

1 Introduction

The ability to predict molecular properties from first principles relies on our capacity to sample Boltzmann-weighted ensembles accurately. Molecular dynamics (MD) and Monte Carlo (MC) simulations provide frameworks for such sampling, offering a means to explore the thermodynamic and kinetic landscapes of complex biophysical systems [1, 2]. Yet, as system complexity grows—such as in the case of drug-protein interactions or enzymatic catalysis—the time scales required to observe biologically relevant events far exceed what is accessible by brute-force simulations. To overcome these limitations, coarse-graining (CG) has emerged as a crucial methodology that simplifies molecular representations by reducing the number of degrees of freedom (DOF), allowing for more efficient simulations while

*Boltzmannstr. 15, 85748 Garching b. München, Germany

preserving key physical properties [3]. There are two main approaches: top-down and bottom-up methods [4, 5]. Top-down methods design CG models to reproduce specific macroscopic properties based on experimental data. In contrast, bottom-up coarse-graining techniques derive CG interactions by defining a mapping from the all-atom, fine-grained (FG) representation to a reduced, coarse-grained description [6]. Typically, this involves lumping multiple atoms into a pseudomolecule, often referred to as “beads”. This inevitably results in a loss of information between the two scales [7, 8] and makes recovering the all-atom structures from the CG representation a challenging back-mapping problem [9–15].

The second necessary component in bottom-up methods is defining a model for the CG coordinates, which should reproduce the equilibrium distribution of the CG DOFs, known as thermodynamic consistency [16]. Many classical CG methods achieve consistency by finding an approximation of the potential of mean force (PMF) or the gradients thereof, i.e., the forces between the CG beads. Direct and Iterative Boltzmann Inversion [17, 18] and Inverse Monte Carlo [19] are commonly used to derive effective CG potentials that reproduce macroscopic behavior. Classical data-driven techniques based on force-matching (multiscale coarse-graining) [20] and relative entropy minimization [21] learn variational models that approximate the PMF. With the rise in deep learning, these methods have been combined with highly expressive neural networks, creating highly expressive CG potentials [22–25]. In Köhler et al., the advantages of both force-matching and relative entropy are combined into a new training method called flow-matching [26]. Data-driven, generative models based on Variational Autoencoders (VAEs) [27] or Generative Adversarial Networks (GANs) [28] are capable of learning CG representations and a back-mapping simultaneously [14, 29–32].

The overwhelming majority of data-based techniques rely on first generating reference data based on long MD simulations, which are assumed to have captured all relevant modes in the configuration space. These are subsequently used to train the postulated CG model. This creates a “chicken-and-egg” problem [33]: CG models rely on all-atom simulation data to learn the system’s behavior, but apart from the insights they provide, they can at best reproduce what is already contained in the data. In other words, we need CG models to efficiently explore new configurations, yet we also need prior all-atom data to train them, creating a circular dependency that limits their ability to discover entirely new modes in the configuration space. Furthermore, we note that these two steps, i.e., data generation and learning, are generally detached from one another. Similar issues are encountered in the automatic discovery of collective variables (CVs) from all-atom, simulation data. These are required by enhanced sampling techniques, such as umbrella sampling [34, 35], metadynamics [36, 37], or adaptive biasing potential methods [38–40], to bias all-atom simulations away from free-energy wells and explore the whole configurational space. Nevertheless, it is questionable whether the CVs discovered can lead to the discovery of other wells beyond those contained in the all-atom simulation data they were trained on.

An alternative to data-driven, bottom-up CG techniques is provided by energy-based methods. These aim to approximate the Boltzmann distribution $p(\mathbf{x})$ using only evaluations of the energy (or interatomic potential) $U(\mathbf{x}) = -\beta^{-1} \log p(\mathbf{x})$ and its derivatives (i.e., interatomic forces). A prominent example is the family of deep generative models known as Boltzmann Generators (BGs) [41], which train normalizing flows (NFs) [42] using a combination of data and energy. BGs have been shown to generalize across different thermodynamic states, such as temperatures and pressures [43, 44]. Recent work on equivariant flows [45] has further demonstrated that incorporating symmetry-preserving architectures into BGs can significantly improve generalization and sampling efficiency. BGs are capable of generating one-shot, independent samples and obtaining unbiased estimates of observables through importance sampling. However, they operate entirely in the all-atom coordinate space and do not employ a coarse-grained description, which limits their scalability and interpretability.

Another line of research avoids reweighting and instead uses normalizing flows as proposals within subsequent Markov chain Monte Carlo (MCMC) schemes [46–49]. Among these, the adaptive Monte Carlo framework of Gabri e et al. trains the NF on-the-fly during sampling, combining local MCMC updates with NF-based nonlocal moves. This hybrid strategy improves mixing efficiency and sampling performance but still relies on having initial data covering all relevant modes; otherwise, the NF may fail to learn unexplored regions of the distribution. In contrast to these approaches, our framework introduces a fully generative, data-free method that operates in a structured latent space, enabling principled coarse-graining, automatic reconstruction of atomistic configurations, and accurate sampling of the Boltzmann distribution—all without requiring precollected trajectories.

The simplest approach for pure energy-based training is minimizing the reverse Kullback-Leibler (KL) divergence. In [50] a normalizing flow model is trained to match the Boltzmann distribution of atomic solids with up to 512 atoms. However, without any dimensionality reduction, the use of this approach is computationally expensive. Also, it is known that the reverse KL-divergence suffers from a mode-seeking behavior [51, 52] which is a problem amplified in higher dimensions, even as those encountered in simple protein systems. In [53], the authors analyze mode collapse during optimization for small atomistic systems and suggest alternative training loss terms. However, they are only able to improve upon a pretrained model. Alternatively, researchers have tried using the α -divergence, which exhibits better

mass-covering properties [54]. The authors additionally used Annealed Importance Sampling (AIS) to facilitate the discovery of new modes. They are the first to learn the Boltzmann distribution of a small protein, alanine dipeptide, purely from its unnormalized density. On the downside, AIS still requires significant computational resources, as mollified versions of the target Boltzmann distribution need to be sampled. Most of these methods operate on global internal coordinates to reduce the complexity of the learning objective. In [55], equivariance is directly incorporated into the flow architecture through internal auxiliary variables, while still operating on Cartesian coordinates. However, the equivariant layers are still expensive, and their models have not been applied to protein systems for pure energy training. Purely machine-learning-based neural samplers such as the Path Integral Sampler (PIS) [56], Denoising Diffusion Sampler (DDS) [57], Time-reversed Diffusion Sampler (DIS) [58], and Iterated Denoising Energy Matching (iDEM) [59], present powerful tools for approximating Boltzmann distributions without molecular dynamics data. While these methods amortize MCMC sampling and can be trained without trajectories, they operate in the full atomistic dimension and do not incorporate physical priors or coarse-graining structure. Moreover, methods relying on stochastic differential equations (SDEs) and diffusion processes often require architectural tricks (e.g., Langevin preconditioning) that hinder simulation-free learning and raise compatibility issues [60].

The main idea of this work is to reparameterize the full atomistic configuration \mathbf{x} using a bijective, learnable transformation that decomposes the system into two components: a set of coarse-grained variables \mathbf{z} , and a complementary set of variables \mathbf{X} . This decomposition is driven by statistical principles: the marginal distribution of \mathbf{z} is encouraged to be **multimodal**, capturing the metastable states one would encounter in molecular dynamics, while the conditional distribution of \mathbf{X} given \mathbf{z} is constrained to be **unimodal**, representing localized thermal fluctuations. Among the infinitely many possible transformations, we seek one that naturally induces this statistical structure through the form of an approximating distribution. We model the joint density over \mathbf{X} and \mathbf{z} as a product of two terms: (i) a flexible, potentially multimodal marginal over \mathbf{z} , parameterized via a normalizing flow, and (ii) a unimodal conditional over \mathbf{X} given \mathbf{z} , such as a Gaussian. These properties are not enforced on the transformation itself but emerge naturally through the design of the learning objective.

To this end, we minimize the Kullback-Leibler divergence between the approximating distribution and the transformed Boltzmann distribution. This leads to the simultaneous achievement of two core objectives:

1. Learn a coarse-graining transformation that captures the statistical structure of the system;
2. Fit an expressive, generative probabilistic model that embeds coarse-graining behavior into its very architecture.

Complementing the statistical formulation is a dynamical interpretation that provides further intuition. The coarse variables \mathbf{z} can be seen as capturing the system’s “slow” degrees of freedom, while the “fast” variables \mathbf{X} , conditioned on \mathbf{z} , rapidly equilibrate. Although the method does not rely on dynamical data, this Perspective highlights the alignment between the statistical structure and physical behavior.

This method provides several appealing features:

- By approximating the full Boltzmann distribution in transformed coordinates, the model achieves thermodynamic consistency at both the coarse-grained and fine-grained levels [61]. This implies that, up to approximation errors, the model can reproduce expectations of arbitrary observables [62].
- The bijective transformation offers a natural avenue to inject physical insight into the selection of coarse-grained variables, thereby enhancing interpretability and generalization in alignment with physical intuition [63].
- Unlike traditional coarse-graining techniques that struggle with the ill-posed inverse problem of back-mapping atomistic details onto coarse-grained configurations, our generative model directly addresses this challenge. Since the mapping is bijective and learned, one can reconstruct full-resolution atomistic configurations, overcoming the “one-to-many” ambiguity inherent in back-mapping [64].
- Crucially, our framework does not require precollected MD trajectories to fit a coarse-grained model. Instead, training relies solely on evaluations of the all-atom force field, eliminating the need for costly and potentially biased data generation that hampers traditional approaches.

Overall, this work introduces a principled, data-free, and physically grounded approach to coarse-grained molecular modeling. It leverages recent advances in probabilistic modeling and generative learning to construct scalable, interpretable, and thermodynamically faithful models of complex molecular systems.

The rest of the paper is structured as follows: In Section 2, we provide a detailed description of the energy-based coarse-graining methodology, highlighting its key principles and algorithmic framework, while discussing comparisons with popular alternatives. We then demonstrate the effectiveness of this approach in Section 3, where we apply it to several model systems: an asymmetric double-well (DW) potential, a Gaussian mixture model (GMM), and the protein

system of alanine dipeptide. Finally, in Section 4, we summarize the main findings of our study and discuss potential avenues for further improvements and enhancements of the method.

2 Methodology

Whether unraveling complex protein folding or magnetic spin interactions, these challenges hinge on the Boltzmann distribution, which serves as the fundamental bridge between interatomic potentials and the probability of microscopic configurations in equilibrium statistical mechanics. The challenge in exploring Boltzmann densities arises from the presence of multiple modes whose locations are generally unknown a priori. As a result, standard MD tools become trapped for a large number of steps combined with the high dimensionality, this renders such calculations impractical or even impossible.

In the following, we propose a generative coarse-graining scheme requiring only evaluations of the interatomic potential and its gradient for training. The core assumption underlying all coarse-graining approaches is that the multimodality of the target Boltzmann distribution is concentrated in a significantly lower-dimensional subspace, or better yet manifold. In a dynamical context, the coordinates along this manifold are often referred to as “slow” degrees of freedom, while the remaining ones are constrained by them [65]. In the statistical setting advocated in this work, the *marginal density* of the “slow” DOFs would still be multimodal (albeit living in lower dimensions), whereas the *conditional density* of the remaining DOFs would be unimodal (and possibly quite narrow). This, in fact, serves as the overarching principle in the ensuing formulations.

2.1 Probabilistic Generative Model

We now formalize the generative coarse-graining framework and describe how the target Boltzmann density is represented under a bijective transformation. We consider an ensemble of n atoms, each of which has coordinates $\mathbf{x}^{(i)} \in \mathbb{R}^3, i = 1, \dots, n$ that are collectively represented with the vector $\mathbf{x} \in \mathcal{M} \subset \mathbb{R}^{d_x}$ where $d_x = 3n$. If $U(\mathbf{x})$ is the interatomic potential, then the target Boltzmann density is defined as:

$$p(\mathbf{x}; \beta) = \frac{e^{-\beta U(\mathbf{x})}}{Z_\beta}, \quad (1)$$

where $\beta = 1/(k_B T)$ is the inverse temperature, k_B the Boltzmann constant, T the temperature, and Z_β the partition function.

We introduce two new sets of DOFs, the meaning of which is explained in the sequel, namely $\mathbf{X} \in \mathcal{X}$ and $\mathbf{z} \in \mathcal{Z}$ through a potentially nonlinear, differentiable, bijective, parameterized mapping:

$$\mathbf{x} = \mathbf{f}_\phi(\mathbf{X}, \mathbf{z}) \quad (2)$$

where $\mathbf{f}_\phi : \mathcal{X} \times \mathcal{Z} \rightarrow \mathcal{M}$ and ϕ are the associated parameters. We provide specific forms for \mathbf{f}_ϕ in the sequel. As illustrated in Figure 1, the “slow” variables \mathbf{z} are modeled with a flexible, potentially multimodal density $q_\theta(\mathbf{z})$, while the “fast” variables \mathbf{X} are modeled conditionally, with a simple unimodal density $q_\theta(\mathbf{X}|\mathbf{z})$. Together, they are mapped to the all-atom coordinates \mathbf{x} through the learnable bijective transformation \mathbf{f}_ϕ .

Since $\dim(\mathbf{x}) = \dim(\mathbf{z}) + \dim(\mathbf{X})$ the partition of the arguments of \mathbf{f}_ϕ requires only deciding a priori about $\dim(\mathbf{z})$. We note that for a system for which the user has no prior knowledge, $\dim(\mathbf{z})$ will need to be manually adjusted based on model results. An automatic way to score and potentially refine trained models based on $\dim(\mathbf{z})$ is discussed in the Conclusions (Section 4). The corresponding density in the $\mathcal{X} \times \mathcal{Z}$ -space would be:

$$p_\phi(\mathbf{X}, \mathbf{z}; \beta) = \frac{e^{-\beta U(\mathbf{f}_\phi(\mathbf{X}, \mathbf{z}))}}{Z_\beta} K_\phi(\mathbf{X}, \mathbf{z}) \quad (3)$$

where $K_\phi(\mathbf{X}, \mathbf{z}) = \left| \det \left(\frac{\partial \mathbf{f}_\phi}{\partial (\mathbf{X}, \mathbf{z})} \right) \right|$. This can also be written as:

$$p_\phi(\mathbf{X}, \mathbf{z}; \beta) = \frac{1}{Z_\beta} e^{-\beta U_\phi(\mathbf{X}, \mathbf{z}; \beta)} \quad (4)$$

where:

$$U_\phi(\mathbf{X}, \mathbf{z}; \beta) = U(\mathbf{f}_\phi(\mathbf{X}, \mathbf{z})) - \beta^{-1} \log K_\phi(\mathbf{X}, \mathbf{z}), \quad (5)$$

i.e., the target density is ϕ -dependent.

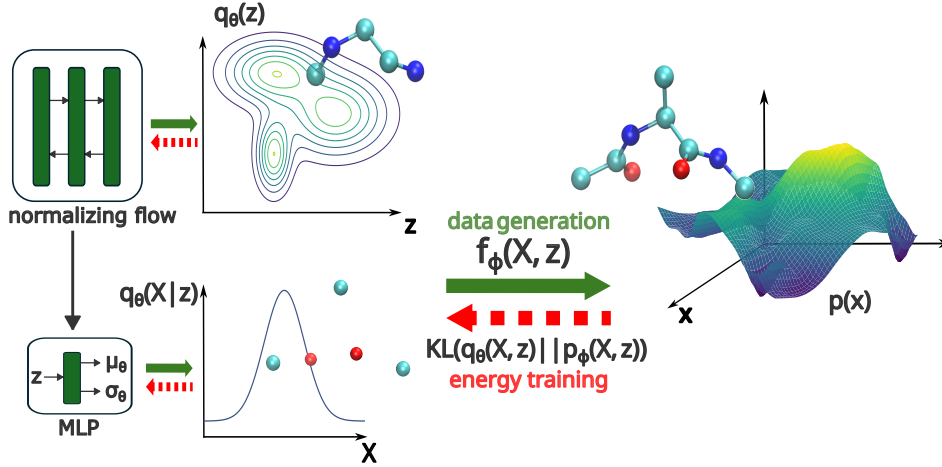


Figure 1: Schematic illustration of the proposed *generative* framework. Two sets of latent coordinates are identified: a) \mathbf{z} with a *multimodal*, learnable density $q_\theta(\mathbf{z})$ corresponding to “slow” DOFs, and b) \mathbf{X} with a *unimodal*, learnable, conditional density $q_\theta(\mathbf{X}|\mathbf{z})$ corresponding to “fast” DOFs modulated by \mathbf{z} . These are combined in order to reconstruct the all-atom DOFs \mathbf{x} through the learnable diffeomorphism f_ϕ .

An infinite number of such transformations arise by varying $\dim(\mathbf{z})$ and the parameters ϕ . We posit that a good set of coarse variables \mathbf{z} should ensure that the **conditional density** $p_\phi(\mathbf{X}|\mathbf{z})$ is **unimodal**, which naturally induces a **multimodal marginal density** $p_\phi(\mathbf{z}) = \int p_\phi(\mathbf{X}, \mathbf{z}; \beta) d\mathbf{X}$ that captures the metastable states of the system. This separation between multimodal and unimodal components underpins the entire generative formulation. From a dynamical point of view, when simulating (\mathbf{X}, \mathbf{z}) -coordinates in an MD/MCMC setting, one would observe that \mathbf{X} would be the “fast” DOFs, which are quickly constrained by \mathbf{z} , whereas the latter would be the “slow” variables exhibiting similar metastable features as \mathbf{x} , albeit in a space of reduced dimension (Figure 1).

In order to discover a transformation that ensures the aforementioned properties, we consider an approximation to $p_\phi(\mathbf{X}, \mathbf{z}; \beta)$ of the form:

$$q_\theta(\mathbf{X}, \mathbf{z}) = q_\theta(\mathbf{z}) q_\theta(\mathbf{X}|\mathbf{z}) \quad (6)$$

Based on the aforementioned objectives, we postulate that:

- $q_\theta(\mathbf{X}|\mathbf{z})$ is a **unimodal** density (e.g., a Gaussian) and
- $q_\theta(\mathbf{z})$ is a potentially **multimodal** density. We model this implicitly by employing a normalizing flow [42] induced by the transformation $g_\theta(\epsilon)$ such that:

$$\mathbf{z} = g_\theta(\epsilon), \quad (7)$$

where $q(\epsilon)$ is the standard Gaussian. As a result:

$$\log q(\epsilon) = \log q_\theta(g_\theta(\epsilon)) + \log J_\theta(\epsilon) \quad (8)$$

where $J_\theta(\epsilon) = |\det(\frac{\partial g_\theta}{\partial \epsilon})|$.

Having specified the model structure, we now turn to the learning objective. To learn both the transformation f_ϕ and the generative approximation q_θ , we minimize the reverse Kullback–Leibler divergence, which encourages q_θ to match the transformed Boltzmann density p_ϕ . Intuitively, this objective ensures that the learned model both identifies a physically meaningful decomposition into “slow” and “fast” variables and provides a powerful generative sampler. In particular, the objective \mathcal{L} is:

$$\begin{aligned} \mathcal{L}(\theta, \phi) &= KL(q_\theta(\mathbf{X}, \mathbf{z}) || p_\phi(\mathbf{X}, \mathbf{z}; \beta)) \\ &= -\langle \log p_\phi(\mathbf{X}, \mathbf{z}; \beta) \rangle_{q_\theta(\mathbf{X}, \mathbf{z})} + \langle \log q_\theta(\mathbf{X}, \mathbf{z}) \rangle_{q_\theta(\mathbf{X}, \mathbf{z})} \\ &= \beta \langle U_\phi(\mathbf{X}, \mathbf{z}; \beta) \rangle_{q_\theta(\mathbf{X}, \mathbf{z})} + \log Z_\beta + \langle \log q_\theta(\mathbf{X}|\mathbf{z}) \rangle_{q_\theta(\mathbf{X}, \mathbf{z})} + \langle \log q_\theta(\mathbf{z}) \rangle_{q_\theta(\mathbf{z})} \end{aligned} \quad (9)$$

We note that in the general case, minimizing the aforementioned KL-divergence simultaneously achieves two objectives:

- learns a diffeomorphic transformation (through ϕ) which defines the coarse variables \mathbf{z} and the reconstruction map.
- learns the generative model q_θ , which produces equilibrium-consistent samples in transformed coordinates.

We further note that the transformation \mathbf{f}_ϕ does not involve dimensionality reduction and once learned can be readily used in order to reconstruct the full atomistic picture, i.e., \mathbf{x} . In combination with q_θ and to the extent this provides a good approximation to the transformed Boltzmann, one can therefore obtain one-shot samples (see Section 2.3).

Importantly, training requires only evaluations of the interatomic potential $U(\mathbf{x})$ (or equivalently U_ϕ) and its gradient (i.e., interatomic forces) [41, 66]. This energy-based training [59] does not require MD trajectories or pregenerated data sets, directly overcoming the traditional ‘‘chicken-and-egg problem’’ faced by data-driven coarse-graining methods.

We consider a particular form of such a bijective map \mathbf{f}_ϕ which is linear, i.e.,

$$\mathbf{x} = \mathbf{A}_\phi \begin{bmatrix} \mathbf{z} \\ \mathbf{X} \end{bmatrix}$$

($d_{\mathbf{x}} = 3n = \dim(\mathbf{x})$, $d_{\mathbf{z}} = \dim(\mathbf{z})$ and $\dim(\mathbf{X}) = d_{\mathbf{x}} - d_{\mathbf{z}}$) where for each atom i with coordinates $\mathbf{x}_{(i)}$ we have:

$$\mathbf{x}_{(i)} = \sum_{j=1}^{d_{\mathbf{z}}} a_{\phi_{i,j}} \mathbf{I} \mathbf{z}_{(j)} + \sum_{j=d_{\mathbf{z}}+1}^{d_{\mathbf{x}}} a_{\phi_{i,j}} \mathbf{I} \mathbf{X}_{(j-d_{\mathbf{z}})} \quad (10)$$

Here, \mathbf{I} denotes the 3×3 identity matrix, and $\mathbf{z}_{(j)}$ and $\mathbf{X}_{(k)}$ are the coordinates of pseudo- \mathbf{z} -atom j and pseudo- \mathbf{X} -atom k , respectively. One can readily show that if:

$$\sum_{j=1}^{d_{\mathbf{x}}} a_{\phi_{i,j}} = 1, \forall i \quad (11)$$

then the corresponding map is **equivariant** to rigid-body motions [29]. The associated \mathbf{A}_ϕ matrix is a right stochastic matrix. We note that typical CG techniques, which lump atoms into bigger, pseudo/virtual-atoms, arise by particular choices of the coefficients $a_{\phi_{i,j}}$ [6, 67]. Unlike these methods, however, our approach learns the mapping and, crucially, retains and models the additional DOFs (i.e., \mathbf{X}), enabling a full reconstruction (back-mapping) of the all-atom coordinates \mathbf{x} . We note that in this case $K_\phi(\mathbf{X}, \mathbf{z}) = \left| \det \left(\frac{\partial \mathbf{f}_\phi}{\partial (\mathbf{X}, \mathbf{z})} \right) \right| = |\det(\mathbf{A}_\phi)|$, which is independent of \mathbf{X}, \mathbf{z} .

A special case of the aforementioned linear map is when \mathbf{A}_ϕ is a *permutation matrix* which arises when $a_{\phi_{i,j}} = 0$ or 1 and there is a single 1 per row and column (in this case $K_\phi(\mathbf{X}, \mathbf{z}) = 1$). Such a map implies a partition of all-atom coordinates \mathbf{x} . An illustration of such a partitioning can be seen in Figure 1 for the alanine dipeptide, where \mathbf{z} represents the coordinates of actual, backbone atoms and \mathbf{X} represents the coordinates of the side-chain atoms.

Remarks:

- Alternative learning objectives, such as the Fisher divergence [68] or the χ^2 -divergence [54, 69], which have been employed in the past and have shown advantages over the reverse KL-divergence adopted herein, could be readily used, but are not pursued in this study. In the subsequent section, we discuss in detail how this KL-divergence can be minimized and the parametrization adopted for the approximation q_θ .
- It is instructive to compare the proposed method with the popular, relative entropy (RE) method [21], which employs the *forward* KL-divergence in the context of coarse-graining. Assuming a coarse-grained map \mathcal{P} , which can be thought of as a partial inverse of \mathbf{f}_ϕ in Equation (2), onto the same, lower-dimensional space $\mathbf{z} = \mathcal{P}(\mathbf{x})$ and the same CG model $q_\theta(\mathbf{z})$, the RE method minimizes the KL-divergence between the (intractable) marginal Boltzmann density of the CG coordinates,

$$p(\mathbf{z}) = \int \delta(\mathbf{z} - \mathcal{P}(\mathbf{x})) p(\mathbf{x}) d\mathbf{x},$$

and its approximant $q_\theta(\mathbf{z})$, as

$$S_{\text{rel}}(\boldsymbol{\theta}) = \text{KL}(p(\mathbf{z}) \parallel q_\theta(\mathbf{z})) = \langle \log p(\mathbf{z}) - \log q_\theta(\mathbf{z}) \rangle_{p(\mathbf{z})},$$

where $S_{\text{rel}}(\boldsymbol{\theta}) \geq 0$ by Gibbs’ inequality, with equality if and only if $p(\mathbf{z}) = q_\theta(\mathbf{z})$ almost everywhere.

During optimization, the first term $\langle \log p(\mathbf{z}) \rangle_{p(\mathbf{z})}$ can be neglected, as it is independent of the model parameters $\boldsymbol{\theta}$. Exploiting the definition of $p(\mathbf{z})$, the objective can be rewritten as an expectation over $p(\mathbf{x})$:

$$S_{\text{rel}}(\boldsymbol{\theta}) = \langle -\log q_\theta(\mathcal{P}(\mathbf{x})) \rangle_{p(\mathbf{x})}.$$

Thus, minimizing the relative entropy corresponds to maximizing the likelihood that the CG model $q_\theta(\mathbf{z})$ reproduces the statistics of the mapped atomistic system, emphasizing coverage of all relevant modes (i.e., mass-covering behavior) rather than focusing on the dominant ones.

However, evaluating this expectation requires sampling from $p(\mathbf{x})$, which is generally intractable and must be approximated via all-atom MD or MCMC simulations. Consequently, the performance of RE-based coarse-graining is fundamentally limited by the quality and completeness of the available data. Furthermore, even if $q_\theta(\mathbf{z})$ provides an excellent approximation to $p(\mathbf{z})$, it does not inherently solve the reconstruction (or back-mapping) problem: additional, often heuristic, steps are necessary to generate consistent all-atom configurations \mathbf{x} from a given \mathbf{z} .

2.2 Training Framework

In this section, we describe the algorithmic steps for training the proposed model, along with a tempering scheme designed to address known challenges in minimizing the reverse KL-divergence [52]. We also provide details on parameters θ and explain why lightweight normalizing flow models can be effective in our formulation.

Given the unimodality assumption for $q_\theta(\mathbf{X}|\mathbf{z})$, we employ a Gaussian:

$$q_\theta(\mathbf{X}|\mathbf{z}) = \mathcal{N}(\mathbf{X}|\mu_\theta(\mathbf{z}), \text{diag}(\sigma_\theta^2(\mathbf{z}))) \quad (12)$$

with mean $\mu_\theta(\mathbf{z})$ and a diagonal covariance matrix with variances given by the vector $\sigma_\theta^2(\mathbf{z})$. This is convenient as it leads to direct reparametrization in the form:

$$\mathbf{X} = \mu_\theta(\mathbf{z}) + \sigma_\theta(\mathbf{z})\epsilon_{\mathbf{X}} = h_\theta(\epsilon_{\mathbf{X}}, \mathbf{z}), \quad (13)$$

where $\epsilon_{\mathbf{X}} \sim q(\epsilon_{\mathbf{X}}) = \mathcal{N}(\mathbf{0}, \mathbf{I})$.

Following Equation (9) and using the reparametrizations implied by the normalizing flow of Equation (7) and in Equation (13), the learning objective $\mathcal{L}(\theta, \phi)$ can be written as:

$$\begin{aligned} \mathcal{L}(\theta, \phi) &= \beta \langle U_\phi(\mathbf{X}, \mathbf{z}; \beta) \rangle_{q_\theta(\mathbf{X}, \mathbf{z})} + \langle \log q_\theta(\mathbf{X}|\mathbf{z}) \rangle_{q_\theta(\mathbf{X}, \mathbf{z})} + \langle \log q_\theta(\mathbf{z}) \rangle_{q_\theta(\mathbf{z})} \\ &= \beta \langle U_\phi(h_\theta(\epsilon_{\mathbf{X}}, g_\theta(\epsilon)), g_\theta(\epsilon)) \rangle_{q(\epsilon, \epsilon_{\mathbf{X}})} + \left\langle \langle \log q_\theta(\mathbf{X}|g_\theta(\epsilon)) \rangle_{q_\theta(\mathbf{X}|g_\theta(\epsilon))} \right\rangle_{q(\epsilon)} \\ &\quad + \langle \log q_\theta(g_\theta(\epsilon)) \rangle_{q(\epsilon)}, \end{aligned} \quad (14)$$

where the partition function is independent of (θ, ϕ) and can therefore be ignored during optimization.

In view of Equation (12), the second term can be expressed (ignoring constants) as

$$\left\langle \langle \log q_\theta(\mathbf{X}|g_\theta(\epsilon)) \rangle_{q_\theta(\mathbf{X}|g_\theta(\epsilon))} \right\rangle_{q(\epsilon)} = -\frac{1}{2} \left\langle \log \det(\text{diag}(\sigma_\theta^2(g_\theta(\epsilon)))) \right\rangle_{q(\epsilon)} \quad (15)$$

We note that the third term (with the help of Equation (8)) can be rewritten as:

$$\langle \log q_\theta(g_\theta(\epsilon)) \rangle_{q(\epsilon)} = \langle \log q(\epsilon) \rangle_{q(\epsilon)} - \langle \log J_\theta(\epsilon) \rangle_{q(\epsilon)}, \quad (16)$$

derivatives of which with respect to θ can be readily obtained from the Jacobian J_θ of the flow.

Gradients of the objective, which are used for its minimization, can be obtained through the application of the chain rule. In particular and with respect to θ , we have:

$$\begin{aligned} \nabla_\theta \mathcal{L}(\theta, \phi) &= \beta \left\langle \frac{\partial U_\phi}{\partial \mathbf{X}} \left(\frac{\partial h_\theta}{\partial \theta} + \frac{\partial h_\theta}{\partial \mathbf{z}} \frac{\partial g_\theta}{\partial \theta} \right) + \frac{\partial U_\phi}{\partial \mathbf{z}} \frac{\partial g_\theta}{\partial \theta} \right\rangle_{q(\epsilon, \epsilon_{\mathbf{X}})} - \frac{1}{2} \left\langle \frac{\partial \log \det(\text{diag}(\sigma_\theta(g_\theta(\epsilon))))}{\partial \theta} \right\rangle_{q(\epsilon)} \\ &\quad - \left\langle \frac{\partial \log J_\theta(\epsilon)}{\partial \theta} \right\rangle_{q(\epsilon)} \end{aligned} \quad (17)$$

The gradient with respect to ϕ is only dependent on the first term of Equation (14) and in view of Equation (5) can be written as:

$$\begin{aligned} \nabla_\phi \mathcal{L}(\theta, \phi) &= \frac{\partial}{\partial \phi} \beta \langle U_\phi(h_\theta(\epsilon_{\mathbf{X}}, g_\theta(\epsilon)), g_\theta(\epsilon)) \rangle_{q(\epsilon, \epsilon_{\mathbf{X}})} \\ &= \beta \left\langle \frac{\partial U}{\partial \mathbf{x}} \frac{\partial \mathbf{f}_\phi(h_\theta(\epsilon_{\mathbf{X}}, g_\theta(\epsilon)), g_\theta(\epsilon))}{\partial \phi} - \frac{1}{\beta} \frac{\partial \log K_\phi(h_\theta(\epsilon_{\mathbf{X}}, g_\theta(\epsilon)), g_\theta(\epsilon))}{\partial \phi} \right\rangle_{q(\epsilon, \epsilon_{\mathbf{X}})} \end{aligned} \quad (18)$$

For a given value of the model parameters (θ, ϕ) , Monte Carlo estimates of the aforementioned gradients, which can be used during training, can be obtained by following the steps below:

1. Generate N independent samples $\{\epsilon^{(i)}\}_{i=1}^N, \{\epsilon_{\mathbf{X}}^{(i)}\}_{i=1}^N$ from the base, standard Gaussian densities $q(\epsilon), q(\epsilon_{\mathbf{X}})$.
2. For each such sample-pair i , compute the:
 - \mathbf{z} -coordinates as $\mathbf{z}^{(i)} = g_{\theta}(\epsilon^{(i)})$, $i = 1, \dots, N$,
 - \mathbf{X} -coordinates as $\mathbf{X}^{(i)} = h_{\theta}(\epsilon_{\mathbf{X}}^{(i)}, \mathbf{z}^{(i)})$, $i = 1, \dots, N$, and
 - \mathbf{x} -coordinates as $\mathbf{x}^{(i)} = \mathbf{f}_{\phi}(\mathbf{X}^{(i)}, \mathbf{z}^{(i)})$.
3. Compute forces on the \mathbf{x} -atoms $\mathbf{F}_{\mathbf{x}}^{(i)} = -\nabla_{\mathbf{x}} U(\mathbf{x}^{(i)})$.
4. Compute the forces on the \mathbf{z} -atoms and \mathbf{X} -atoms :

$$\begin{aligned}\mathbf{F}_{\mathbf{z}}^{(i)} &= \mathbf{F}_{\mathbf{x}}^{(i)} \nabla_{\mathbf{z}} \mathbf{f}_{\phi}(\mathbf{X}^{(i)}, \mathbf{z}^{(i)}) + \beta^{-1} \nabla_{\mathbf{z}} \log K_{\phi}(\mathbf{X}^{(i)}, \mathbf{z}^{(i)}) \\ \mathbf{F}_{\mathbf{X}}^{(i)} &= \beta \mathbf{F}_{\mathbf{x}}^{(i)} \nabla_{\mathbf{X}} \mathbf{f}_{\phi}(\mathbf{X}^{(i)}, \mathbf{z}^{(i)}) + \beta^{-1} \nabla_{\mathbf{X}} \log K_{\phi}(\mathbf{X}^{(i)}, \mathbf{z}^{(i)})\end{aligned}\quad (19)$$

5. Approximate θ -gradient (see Equation (17)):

$$\begin{aligned}\nabla_{\theta} \mathcal{L}(\theta, \phi) &\approx \frac{1}{N} \sum_{i=1}^N -\beta \mathbf{F}_{\mathbf{X}}^{(i)} \left(\nabla_{\theta} h_{\theta}(\epsilon_{\mathbf{X}}^{(i)}, \mathbf{z}^{(i)}) + \nabla_{\mathbf{z}} h_{\theta}(\epsilon_{\mathbf{X}}^{(i)}, \mathbf{z}^{(i)}) \nabla_{\theta} g_{\theta}(\epsilon^{(i)}) \right) \\ &\quad - \beta \left(\mathbf{F}_{\mathbf{z}}^{(i)} \nabla_{\theta} g_{\theta}(\epsilon^{(i)}) \right) - \frac{1}{2} \nabla_{\theta} \log \det(\text{diag}(\sigma_{\theta}^2(\mathbf{z}^{(i)}))) - \nabla_{\theta} \log J_{\theta}(\epsilon^{(i)})\end{aligned}\quad (20)$$

6. Approximate ϕ -gradient (see Equation (18)):

$$\nabla_{\phi} \mathcal{L}(\theta, \phi) \approx \frac{1}{N} \sum_{i=1}^N -\beta \mathbf{F}_{\mathbf{x}}^{(i)} \nabla_{\phi} \mathbf{f}_{\phi}(\mathbf{X}^{(i)}, \mathbf{z}^{(i)}) - \nabla_{\phi} \log K_{\phi}(\mathbf{X}^{(i)}, \mathbf{z}^{(i)})\quad (21)$$

Remarks:

- The calculation above of the forces $\mathbf{F}_{\mathbf{z}}^{(i)}$ and $\mathbf{F}_{\mathbf{X}}^{(i)}$ ensures that we do not evaluate the potential energy multiple times, which is often the most costly aspect of the gradient evaluation. We further note that the second term in Equation (19) vanishes for transformations of the form $\mathbf{x} = \mathbf{A}_{\phi} [\mathbf{z} \quad \mathbf{X}]^{\top}$, which we introduced earlier as the Jacobian $K_{\phi}(\mathbf{X}, \mathbf{z}) = |\det(\mathbf{A}_{\phi})|$ is independent of \mathbf{X} and \mathbf{z} .
- The proposed method shares some similarities with Boltzmann Generators, as it uses normalizing flows to approximate the Boltzmann distribution. However, there are some key differences. Boltzmann Generators[41] combine data-based and energy-based training of normalizing flows with reweighting to obtain unbiased samples from the target Boltzmann distribution. In contrast, we discover a density $q_{\theta}(\mathbf{z})$ that lives in a lower-dimensional space compared to the original Boltzmann distribution $p(\mathbf{x})$ but nevertheless encompasses the multiple modes that are present in the latter and which are a priori unknown. We do so by stabilizing energy training with an adaptive tempering scheme. Some BGs employ a partitioning of coordinates (e.g., backbone and side chain atoms) in the neural network architecture of the flow model and in the construction of the internal coordinates in order to improve training efficiency. Our method builds the partition of “slow” and “fast” DOFs directly into the probabilistic framework in the form of a unimodal conditional distribution $q_{\theta}(\mathbf{X}|\mathbf{z})$. This simplifies the learning process and pushes the multimodality into the aforementioned density $q_{\theta}(\mathbf{z})$.
- The Monte Carlo estimates of the gradients of the training objective in Equations (20) and (21) are used to update the parameters (θ, ϕ) using a Stochastic Gradient Descent (SGD) scheme. In particular, we use the ADAM optimizer [70] with parameters $\beta_1 = 0.99$, $\beta_2 = 0.999$, and $\epsilon_{\text{ADAM}} = 1.0 \times 10^{-8}$.

The minimization of the reverse KL-divergence as in Equation (14) is fraught with well-documented computational difficulties [71–73]. In particular, it exhibits a *mode-seeking* behavior, which in the context of multimodal target densities considered, can be particularly deleterious as it can lead to approximations $q_{\theta}(\mathbf{X}, \mathbf{z})$ that miss some important mode(s) [52]. The reverse KL-divergence penalizes q_{θ} for placing probability mass, where p_{ϕ} is small. As a result, q_{θ} tends to concentrate on regions where p_{ϕ} is large, while avoiding areas of low support. This exclusion of low-density regions of p_{ϕ} gives rise to its mode-seeking behavior [74]. The most important mitigating factor in the proposed formulation, as compared to others that have used the reverse KL [41, 50, 53], is that training is carried out in a (much)

Algorithm 1 Training algorithm with adaptive tempering

```

1: Input: Target inverse temperature  $\beta_{\text{target}}$ , maximal relative KL increase  $\delta KL_{\text{max}}$ , maximal  $\beta$ -increment  $\Delta\beta_{\text{max}}$ ,
   learning rate  $\eta_{\text{SGD}}$ .
2: Initialize: Parameters  $(\theta, \phi)$ ,  $\beta_0 \leftarrow 0$ , adaptive tempering counter  $k \leftarrow 0$ .
3: while  $\beta_k < \beta_{\text{target}}$  do ▷ Outer tempering loop
4:   while not converged do ▷ Inner optimization loop
5:     Compute Monte Carlo estimates of gradients  $\nabla_{\theta}\mathcal{L}$  and  $\nabla_{\phi}\mathcal{L}$  ▷ see Equations (20) and (21)
6:     Update parameters:  $\theta \leftarrow \theta + \eta_{\text{SGD}} \cdot \nabla_{\theta}\mathcal{L}$ 
7:     Update parameters:  $\phi \leftarrow \phi + \eta_{\text{SGD}} \cdot \nabla_{\phi}\mathcal{L}$ 
8:   end while
9:   Compute increment  $\Delta\beta_k$  ▷ see Equation (23)
10:  Update inverse temperature:  $\beta_{k+1} \leftarrow \beta_k + \Delta\beta_k$ 
11:  Increment counter:  $k \leftarrow k + 1$ 
12: end while

```

lower-dimensional space \mathcal{Z} as compared to the original Boltzmann. The second mitigating factor is a tempering scheme that we employ, the effectiveness of which is illustrated empirically in the numerical experiments (Section 3.1). We note that for $\beta \rightarrow 0$ (or equivalent $T \rightarrow \infty$), the target Boltzmann is effectively uniform and unimodal. As β is slowly increased, the modes become more pronounced, but as long as this is done carefully, the approximation can track them. While the shape of the modes may change, updates to θ can easily account for it. Furthermore, the approximation obtained at a certain β serves as a good initial guess for subsequent β . An additional benefit of such a strategy is that one obtains a CG generative model for all intermediate β values considered.

To this end, we employ an adaptive, information-theoretic scheme that automatically determines the sequence of β values, starting from 0 and progressing to the target β_{target} , ensuring a smooth transition that captures all relevant modes [66]. Let $q_{\theta}(\mathbf{X}, \mathbf{z})$ be the optimal approximation to the target $p_{\phi}(\mathbf{X}, \mathbf{z}; \beta_k)$ for the current $\beta = \beta_k$ at step k . Our goal is to determine $\beta_{k+1} = \beta_k + \Delta\beta_k$, i.e., to identify $\Delta\beta_k > 0$ so as $p_{\phi}(\mathbf{X}, \mathbf{z}; \beta_{k+1})$ does not differ substantially from $p_{\phi}(\mathbf{X}, \mathbf{z}; \beta_k)$ and one can readily transition to the new optimal approximation q_{θ} . We note that even though the parameters ϕ are also updated at the new β_{k+1} in order to find their new optimal values, this is not considered in the adaptivity metrics.

For this purpose, we employ the relative change in the KL-divergence used as the learning objective, namely:

$$\delta KL_k(\Delta\beta_k) = \frac{KL(q_{\theta}(\mathbf{X}, \mathbf{z})||p_{\phi}(\mathbf{X}, \mathbf{z}; \beta_{k+1})) - KL(q_{\theta}(\mathbf{X}, \mathbf{z})||p_{\phi}(\mathbf{X}, \mathbf{z}; \beta_k))}{KL(q_{\theta}(\mathbf{X}, \mathbf{z})||p_{\phi}(\mathbf{X}, \mathbf{z}; \beta_k))} \quad (22)$$

We note that when $\beta_{k+1} \rightarrow \beta_k$, $\delta KL_k \rightarrow 0$, and as β_{k+1} deviates from β_k , we would expect δKL_k to increase. Hence, we define an upper bound δKL_{max} and select $\Delta\beta_k$ such that

$$\Delta\beta_k = \min\{\delta KL_k(\Delta\beta_k) = \delta KL_{\text{max}}, \Delta\beta_{\text{max}}, \beta_{\text{target}} - \beta_k\} \quad (23)$$

where $\Delta\beta_{\text{max}}$ is another user-defined threshold and β_{target} is the maximum β (or equivalently, minimal absolute temperature) of interest. Values for the parameters of Equation (23) are reported in Section 3. In the Appendix A, we provide details regarding the numerical approximation of δKL_k , which is based on Importance Sampling.

We finally provide an overview of the data-free training of the generative model proposed in pseudo-Algorithm 1, where the outer loop increments $\Delta\beta_k$ according to the adaptive scheme described above, while the inner loop updates the model parameters θ and ϕ using Stochastic Gradient Descent and the aforementioned, Monte Carlo estimates of the gradients. A combination of gradient norm reduction, loss change, and maximum iterations was used to detect convergence.

2.3 Predictions

Once our model is fully trained, we can generate one-shot samples, which approximately follow the target Boltzmann distribution with the following steps:

1. Generate N samples $\{\epsilon^{(i)}\}_{i=1}^N$ from the base density $q(\epsilon)$.
2. Compute the \mathbf{z} -coordinates as $\mathbf{z}^{(i)} = g_\theta(\epsilon^{(i)})$, $i = 1, \dots, N$.
3. Sample the conditional $\mathbf{X}^{(i)} \sim q_\theta(\mathbf{X}|\mathbf{z}^{(i)})$.
4. Transform back to the \mathbf{x} -coordinates as $\mathbf{x}^{(i)} = \mathbf{f}_\phi(\mathbf{X}^{(i)}, \mathbf{z}^{(i)})$.

Furthermore, we can evaluate the free energy $A(\mathbf{z}) = -\beta^{-1} \log q_\theta(\mathbf{z})$ to calculate transition paths and energy differences in the latent \mathcal{Z} -space. Moreover, we do not only obtain one model for the target Boltzmann distribution, but for each intermediate distribution chosen during tempering. This allows us to generate samples at each β_k for which we converged during training. We note that $q_\theta(\mathbf{z})$ provides, in essence, a thermodynamically consistent projection of the original Boltzmann distribution, which can be further processed in order to learn, e.g., collective variables [33, 75] or as the starting point for further coarse-graining operations, which can proceed in a hierarchical fashion. Unbiased estimates of any physical observable $a(\mathbf{x})$ with respect to the Boltzmann density $p(\mathbf{x}; \beta)$, and for any β in the sequence considered during training, can be calculated using Importance Sampling as:

$$\begin{aligned}
\langle a(\mathbf{x}) \rangle_{p(\mathbf{x}; \beta)} &= \int a(\mathbf{x}) p(\mathbf{x}; \beta) d\mathbf{x} \\
&= \int a(\mathbf{x}) \frac{e^{-\beta U(\mathbf{x}; \beta)}}{Z_\beta} d\mathbf{x} \\
&= \int a(\mathbf{f}_\phi(\mathbf{X}, \mathbf{z})) \frac{e^{-\beta U_\phi(\mathbf{X}, \mathbf{z}; \beta)}}{Z_\beta} d\mathbf{X} d\mathbf{z} \\
&= \int a(\mathbf{f}_\phi(\mathbf{X}, \mathbf{z})) w(\mathbf{X}, \mathbf{z}) q_\theta(\mathbf{X}, \mathbf{z}) d\mathbf{X} d\mathbf{z} \\
&\approx \sum_{m=1}^M W^{(m)} a(\mathbf{f}_\phi(\mathbf{X}^{(m)}, \mathbf{z}^{(m)})), \quad (\mathbf{X}^{(m)}, \mathbf{z}^{(m)}) \sim q_\theta(\mathbf{X}, \mathbf{z}), \tag{24}
\end{aligned}$$

where $w(\mathbf{X}, \mathbf{z}) = \frac{1}{Z_\beta} \frac{e^{-\beta U_\phi(\mathbf{X}, \mathbf{z}; \beta)}}{q_\theta(\mathbf{X}, \mathbf{z})}$ and $W^{(m)}$ are the normalized IS weights computed as $W^{(m)} = \frac{w^{(m)}}{\sum_{m'=1}^M w^{(m'')}}$ using the unnormalized weights $w^{(m)} = \frac{e^{-\beta U_\phi(\mathbf{X}^{(m)}, \mathbf{z}^{(m)}; \beta)}}{q_\theta(\mathbf{X}^{(m)}, \mathbf{z}^{(m)})}$. Furthermore, as long as the dominant modes have been captured by q_θ , it could serve as the starting point in a bridging density, e.g., $q_\theta^{(1-\gamma)} p_\phi^\gamma$, $\gamma \in [0, 1]$ that would quickly be explored with the help of Annealed Importance Sampling (AIS) [76], or even better, Sequential Monte Carlo (SMC) [77].

2.4 Model Specification

The basis of the formulation is the density $q_\theta(\mathbf{z})$ with respect to the CG DOFs \mathbf{z} , which should exhibit the requisite expressivity in order to adapt to the target marginal $p_\phi(\mathbf{z})$. It is vital that the model is capable of capturing all the different metastable states of the system and, therefore, has to be able to account for the multimodality in the energy landscape. A popular choice to model an arbitrary multimodal distribution is a normalizing flow [42]. These combine a sequence of bijective, deterministic transformations to convert a simple base distribution into any complex distribution, as shown in Equation (7).

We use coupling layers on the Cartesian coordinates of the system, similar to Real NVP [78] but substitute the affine layers with monotonic rational-quadratic splines [79]. These splines have fully differentiable and invertible mappings, while allowing highly expressive transformations. This makes them a perfect candidates to capture complex multimodal distributions. They have been used in many different forms in the context of Boltzmann generators and normalizing flows for Boltzmann distributions [51, 55, 80, 81]. We emphasize, however, that the strength of the proposed framework primarily draws from the bijective decomposition and the projection of the multimodality onto reduced coordinates \mathbf{z} . As a result, we can employ a much more lightweight and smaller neural network architecture, reducing the computational effort during training. It would be interesting to apply our methods with SE(3) equivariant coupling flows [55] as incorporating symmetries into the model directly can improve training efficiency and generalization [45, 82–84].

As the neural splines are defined only in an interval, Durkan et al. transform values outside the interval as the identity, resulting in linear tails, by setting the boundary derivatives to 1. We change the base distribution $q(\epsilon)$ to be a truncated normal distribution defined in the interval of the splines. Therefore, all generated samples are guaranteed to stay inside the support of the splines. This is particularly useful in the early stages of optimization, when q_θ provides a poor approximation.

The second part of our framework focuses on the conditional distribution $q_\theta(\mathbf{X}|\mathbf{z})$ in Equation (12). We model the mean $\mu_\theta(\mathbf{z})$ and standard deviation $\sigma_\theta(\mathbf{z})$, which depend on the “slow” DOFs \mathbf{z} and must be flexible enough to capture this dependence. This density is unimodal and generally easier to learn than the multimodal density $q_\theta(\mathbf{z})$. To parametrize $\mu_\theta(\mathbf{z})$ and $\log \sigma_\theta(\mathbf{z})$, we employ a simple feedforward neural network, specifically a multilayer perceptron (MLP), details of which are contained in Section 3.

Lastly, the diffeomorphism \mathbf{f}_ϕ in Equation (2) is learned using the aforementioned right stochastic matrix \mathbf{A}_ϕ . To enforce the property in Equation (11) that guarantees equivariance to rigid-body motions, we employ a row-wise softmax transformation to the parameter matrix ϕ :

$$(\mathbf{A}_\phi)_{ij} = \frac{\exp(\phi_{ij})}{\sum_{k=1}^N \exp(\phi_{ik})}$$

We implement our models using the `flowjax` [85] package for continuous distributions, bijective transformations, and normalizing flows using `equinox` [86] and `JAX` [87]. Additional details can be found in the respective numerical illustrations in the next section. The code will be made available upon publication at https://github.com/pkmtum/energy_coarse_graining_flow.

3 Numerical Illustrations

The following section demonstrates the capabilities of the proposed method for three use cases. First, we consider two synthetic examples: a two-dimensional double-well potential and a multimodal Gaussian mixture model. The third problem involves the alanine dipeptide.

3.1 Double-Well

In this section, we apply our framework to a 2D double-well potential $U(\mathbf{x})$, where the two metastable states are separated by a high-energy barrier. Traditional methods, such as MD or MCMC, struggle to discover both modes in the target Boltzmann distribution since the second mode exhibits a much lower probability. The particular form of the potential is similar to the one used by Noé et al. and is depicted on the left side of Figure 4:

$$U(\mathbf{x}) = \frac{1}{4}x_1^4 - 3x_1^2 + x_1 + \frac{1}{2}x_2^2 \quad (25)$$

We observe that the x_1 -direction distinguishes between the two modes and is the slow reaction coordinate of the system. This implies that x_1 dictates the multimodality in the Boltzmann distribution. Therefore, we would expect that our model discovers a new set of coordinates (z, X) that strongly correlate with x_1 and x_2 respectively. We use a 2×2 right stochastic matrix \mathbf{A}_ϕ to model the transformation:

$$\mathbf{f}_\phi(X, z) = \mathbf{A}_\phi \begin{bmatrix} z \\ X \end{bmatrix} = \begin{bmatrix} a_1 & 1 - a_1 \\ a_2 & 1 - a_2 \end{bmatrix} \begin{bmatrix} z \\ X \end{bmatrix} = \begin{bmatrix} x_1 \\ x_2 \end{bmatrix} = \mathbf{x}, \quad (26)$$

where $\dim(z) = \dim(X) = \dim(x_1) = \dim(x_2) = 1$. In this case, we have parametrized the sought matrix \mathbf{A}_ϕ with respect to $a_1, a_2 \in [0, 1]$.

We employ a normalizing flow model with the hyperparameters specified in Table 1. Since coupling layers do not operate on one-dimensional inputs, we use only the rational-quadratic spline layers without the dimensional split of the coupling layers. An MLP models the μ_θ and σ_θ of the conditional distribution $q_\theta(X|z) = \mathcal{N}(X|\mu_\theta(z), \sigma_\theta^2(z))$ with hyperparameters in Table 2. The base distribution of the flow $q(\epsilon)$ is a truncated standard normal distribution in the interval $[-5, 5]$. We optimize the parameters using the ADAM optimizer [70] with a learning rate $\eta_{\text{SGD}} = 0.001$. We train for $L = 100$ update steps per tempering step with $N = 500$ samples to estimate the gradients in Equations (20) and (21) (see Algorithm 1). We found that training at the initial $\beta_0 \approx 0$ for an additional 4900 steps results in a more stable convergence of the learned map \mathbf{A}_ϕ and a more successful tempering scheme.

Table 1: Normalizing Flow Architecture for g_θ (see Equation (7)) in the Double-Well Potential Example.

Flow layers	MLP layers	MLP width	RQS knots	RQS Interval
6	2	32	8	$[-5, 5]$

Table 2: MLP Architecture Used for Mean and Variance of $q_\theta(X|z)$ (see Equation (13)).

MLP layers	MLP width	Activation layer
2	32	ReLU

Before assessing predictive accuracy, we first discuss the learned transformation of the original DOFs (Equation (26)). In Figure 2, we plot the KL-based learning objective of Equation (9) for different values of a_1, a_2 (and for the optimal $q_\theta(X, z)$ learned). We observe the evolution of the parameters a_1, a_2 from their initial values, which were randomly selected, to the minimum in the bottom right corner corresponding to $a_1 = 1, a_2 = 0$, i.e., to $z = x_1$ and $X = x_2$. The optimization was carried out with the constraint $\det(\mathbf{A}_\phi) > 0$ [88, 89]. Similar results are obtained for any other initialization point in the lower triangle, which corresponds to $\det(\mathbf{A}_\phi) > 0$.

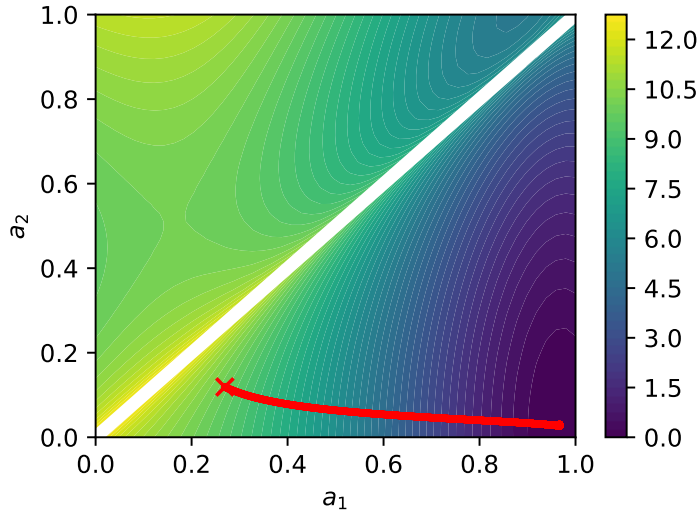


Figure 2: Contour lines of the reverse KL-divergence in Equation (9) for different value pairs (a_1, a_2) of the right stochastic matrix \mathbf{A}_ϕ in Equation (26). The red \times represents the starting values, and the red line represents the values during training. The final learned transformation, based on \mathbf{A}_ϕ^{-1} , is $z = 1.03 \cdot x_1 - 0.04 \cdot x_2$ and $X = -0.03 \cdot x_1 + 1.03 \cdot x_2$.

As explained in the previous sections, energy training is highly prone to mode locking, which for this potential occurs either at $x_1 \approx -2.5$ (most often) or at $x_1 \approx +2.5$. To mitigate this behavior, we use the adaptive tempering scheme proposed (see Algorithm 1) with an inverse temperature step of $\Delta\beta_{\max} = 0.05$, maximum change in KL-divergence $\delta KL_{\max} = 0.1$, and target $\beta_{\text{target}} = 1$.

Figure 3 provides insight into the tempering scheme by displaying predictions from the model trained at various intermediate β . The left column shows the reference potential energy $\beta U(x_1, x_2 = 0) = -\log p(x_1, x_2 = 0)$ and the predicted potential $U_\theta(X, z) = -\log q_\theta(X, z)$, which can be transformed to $U_\theta(x_1, x_2 = 0) = -\log q_\theta(\mathbf{f}_\phi^{-1}(x_1, x_2 = 0)) + \log K_\phi$ using Equation (5). On the right column, we assess the accuracy in predicting the marginal density (and indirectly the corresponding free-energy) of the known collective variable, i.e., x_1 . We observe that the proposed method produces a highly accurate approximation at the target and also at intermediate temperatures. As one would expect, for the initial $\beta_0 = 0.01$, the target density is close to a uniform. This accelerates the exploration of the configurational space, since the barriers between the modes are minute and easily learned by our model. As the inverse temperature β increases, the presence of the two modes becomes more pronounced, but can be gradually captured by the flow model. At the target $\beta_{\text{target}} = 1$, the mode at $x_1 \approx -2.5$ has around 99% of the probability mass.

Furthermore, we can readily obtain all-atom samples $\mathbf{x} = (x_1, x_2)$ as described in Section 2.3. We obtain samples from the reference Boltzmann using a NUTS sampler [90] initialized at a randomly selected location. We observe that we need $\mathcal{O}(10^8)$ energy/force evaluations in order to achieve good statistical accuracy. In Figure 4, we depict two two-dimensional histograms at the target temperature $\beta_{\text{target}} = 1$ from the reference samples and independent samples drawn from the trained approximation $q_\theta(X, z)$ (see Section 2.3).

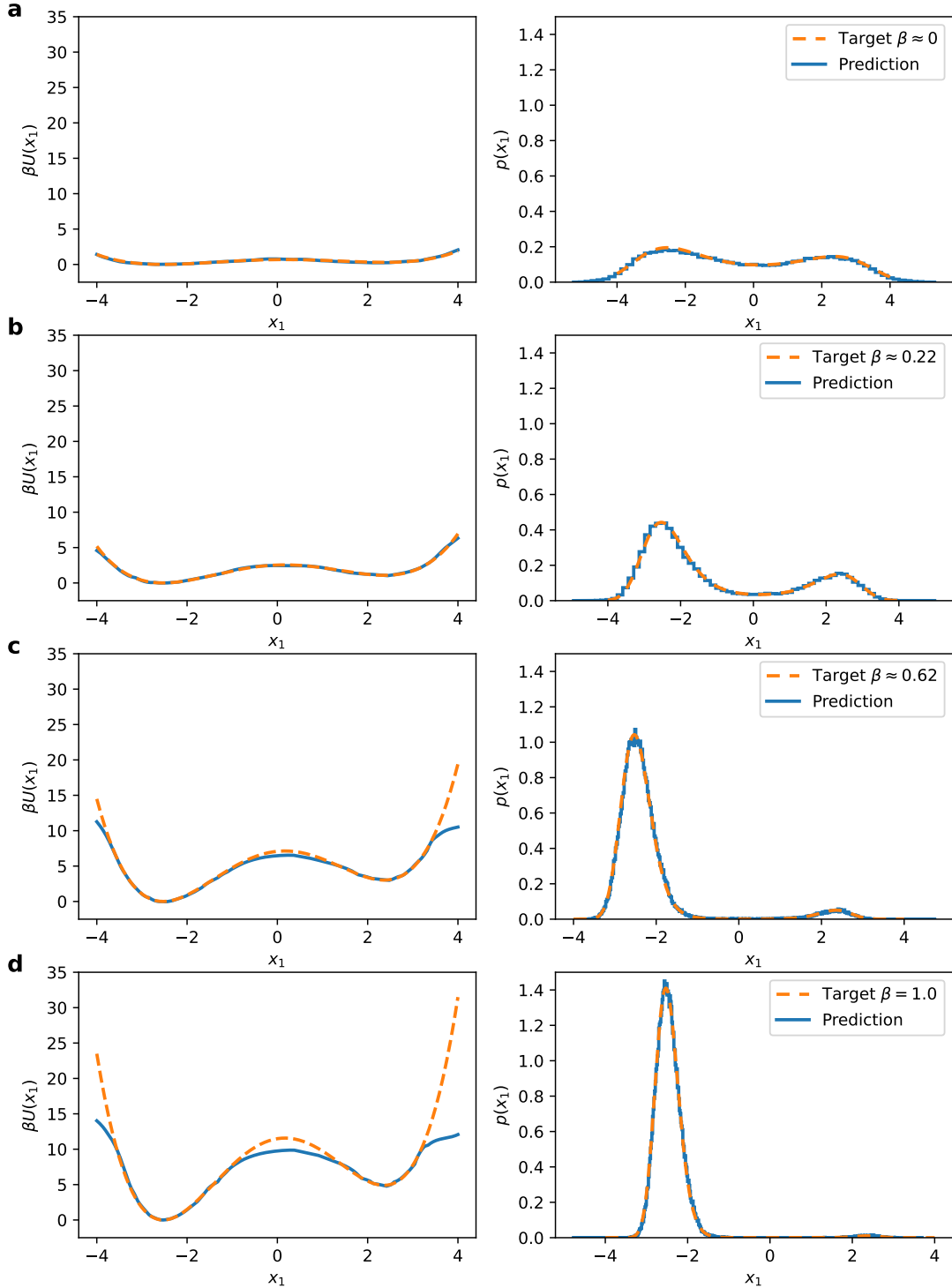


Figure 3: Left: Effective potential (PMF) $\beta U(x_1, x_2 = 0) = -\log p(x_1, x_2 = 0)$ (orange) and the predicted $U_\theta(x_1, x_2 = 0) = -\log q_\theta(\mathbf{f}_\phi^{-1}(x_1, x_2 = 0)) + \log K_\phi$ (blue) during training. Right: Histogram of samples from the marginal $p(x_1)$ (orange) and the predicted model $q_\theta(X, z)$ (blue). Results are shown at the inverse temperatures (a) $\beta \approx 0$, (b) $\beta = 0.2$, (c) $\beta = 0.6$, and (d) $\beta = 1$.

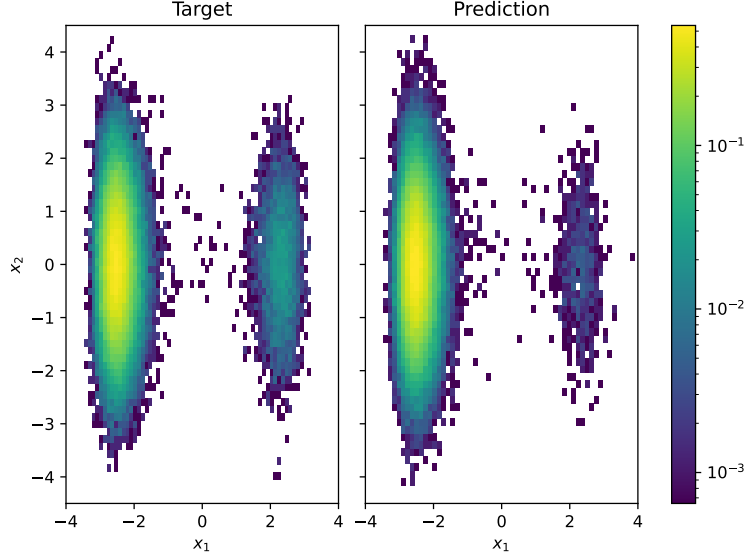


Figure 4: (Left) Histogram of all-atom samples from the target Boltzmann of Equation (25) and (Right) from the energy-trained approximation $q_{\theta}(\mathbf{X}, \mathbf{z})$ ($\beta_{\text{target}} = 1$).

We finally note that training our model required $\mathcal{O}(10^6)$ energy/force evaluations, i.e., approximately 2 of magnitude less than the reference simulations. With this computational cost, we obtain accurate approximations of the target Boltzmann densities at all intermediate temperatures, from which we can generate *independent, one-shot* samples, in contrast to the correlated samples obtained from the reference NUTS simulations.

3.2 Gaussian Mixture Model

In the second synthetic example, we consider a multimodal target density that arises from a Gaussian mixture model (GMM) with three distinct modes. In particular, we partition the all-atom coordinates \mathbf{x} as $(\mathbf{x}_{\mathbf{X}}, \mathbf{x}_{\mathbf{z}})$ and write $p(\mathbf{x}_{\mathbf{X}}, \mathbf{x}_{\mathbf{z}}) = p(\mathbf{x}_{\mathbf{X}}|\mathbf{x}_{\mathbf{z}}) p(\mathbf{x}_{\mathbf{z}})$ where:

$$p(\mathbf{x}_{\mathbf{z}}) = \sum_{k=1}^3 w_k \mathcal{N}(\mathbf{x}_{\mathbf{z}}|\mathbf{m}_k, \Sigma_k) \quad (27)$$

is the mixture of three Gaussians with equal weights $w_k = 1/3$, means \mathbf{m}_k randomly sampled from a uniform distribution between $[-1, 1]^{\dim(\mathbf{z})}$, and a diagonal covariance $\Sigma_k = \text{diag}(0.01)$. The conditional is defined as

$$p(\mathbf{x}_{\mathbf{X}}|\mathbf{x}_{\mathbf{z}}) = \mathcal{N}(\mathbf{x}_{\mathbf{X}}|\mathbf{B}\mathbf{x}_{\mathbf{z}}, \mathbf{S}), \quad (28)$$

where the entries of the matrix \mathbf{B} were sampled from a standard normal distribution and the covariance is diagonal $\mathbf{S} = \text{diag}(0.01)$. We emphasize that this prepartitioning of \mathbf{x} is *not* used in the training of our model, but is solely employed for the construction of the target Boltzmann density.

In terms of dimensions, we consider two different settings: a) $\dim(\mathbf{x}) = 4$ with $\dim(\mathbf{x}_{\mathbf{z}}) = 2$, $\dim(\mathbf{x}_{\mathbf{X}}) = 2$ and, b) $\dim(\mathbf{x}) = 20$ with $\dim(\mathbf{x}_{\mathbf{z}}) = 10$, $\dim(\mathbf{x}_{\mathbf{X}}) = 10$. The lower-dimensional setting is chosen for ease of visualization, whereas the higher-dimensional setting presents substantially greater challenges for training.

Table 3: Normalizing Flow Architecture for g_{θ} (see Equation (7)) in the GMM Example.

Coupling layers	MLP layers	MLP width	RQS knots	RQS Interval	$\dim(\theta)$
8	2	40	8	$[-4, 4]$	23272 ($d_{\mathbf{x}} = 4$) 62600 ($d_{\mathbf{x}} = 20$)

The details of the architecture of the normalizing flow model used for $q_{\theta}(\mathbf{z})$ can be found in Table 3 and for the conditional $q_{\theta}(\mathbf{X}|\mathbf{z})$ in Table 4. The parameters (θ, ϕ) are optimized using the ADAM optimizer with a learning rate $\eta_{\text{SGD}} = 0.001$. We estimate expectations of the gradients with $N = 10000$ samples.

Table 4: MLP Architecture Used for Mean and Variance of $q_\theta(\mathbf{X}|\mathbf{z})$ (see Equation (13)).

MLP layers	MLP width	Activation layer	dim(θ)
2	40	ReLU	1924 ($d_x = 4$) 2900 ($d_x = 20$)

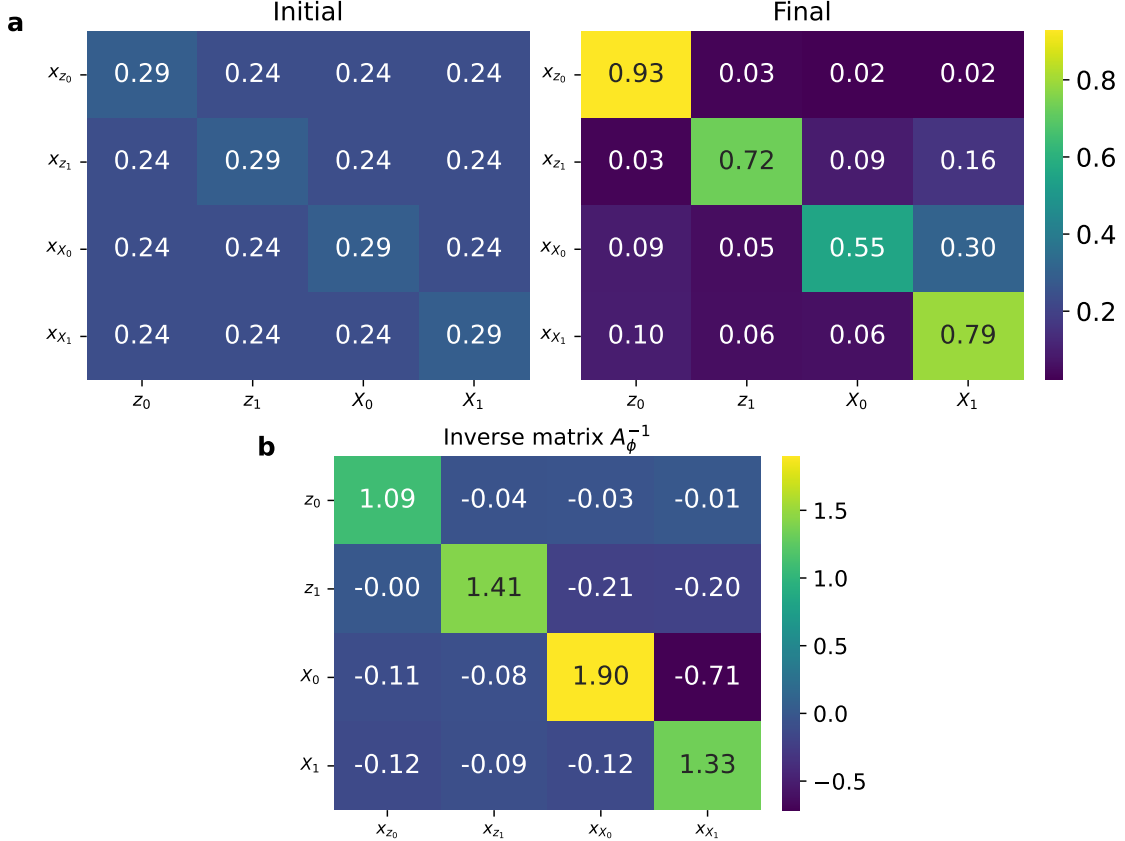


Figure 5: (a) Right stochastic matrix \mathbf{A}_ϕ at (left) initialization and (right) at target inverse temperature $\beta = 1$. (b) Inverse matrix \mathbf{A}_ϕ^{-1} at $\beta = 1$.

The adaptive tempering proposed is carried out with $\delta KL_{\max} = 0.1$, $\Delta\beta_{\max} = 0.02$, and we use 10000 samples to estimate the KL-divergence. We train for $L = 1000$ epochs at each temperature until we reach the target $\beta_{\text{target}} = 1$. We note that convergence for the initial $\beta_0 = 0.001$ is crucial for the success of the tempering scheme. Therefore, we train for an additional 19000 update steps at this initial β .

For the lower-dimensional case ($\dim(\mathbf{x}) = 4$), we show in Figure 5 the initial and learned transformation matrix \mathbf{A}_ϕ as well as its inverse \mathbf{A}_ϕ^{-1} (for $\dim(\mathbf{z}) = 2 = \dim(\mathbf{x}_z)$). The initial, right-stochastic matrix \mathbf{A}_ϕ has as uniform entries as possible (while ensuring that $\det(\mathbf{A}_\phi) > 0$), which is achieved by adding a small positive number to the diagonal terms. We note that the optimal \mathbf{A}_ϕ identified is diagonally dominant, and this can be seen more clearly in its inverse. The learned “slow” variables \mathbf{z} are mostly associated with the \mathbf{x}_z -coordinates, along which the target is multimodal by construction (see Equation (27)). Similarly, \mathbf{X} are associated primarily with \mathbf{x}_X (see Equation (28)).

In Figure 6, the \mathbf{x}_z -coordinates corresponding to independent samples drawn from the trained model, i.e., $q_\theta(\mathbf{X}, \mathbf{z})$ and transformation \mathbf{f}_ϕ , are depicted against contour lines from the target distribution $p(\mathbf{x}_z)$ above. Underneath, we compare the marginals of the \mathbf{x}_z -coordinates. We observe that our model can accurately jointly and marginally capture all three modes of the GMM (see Equation (27)).

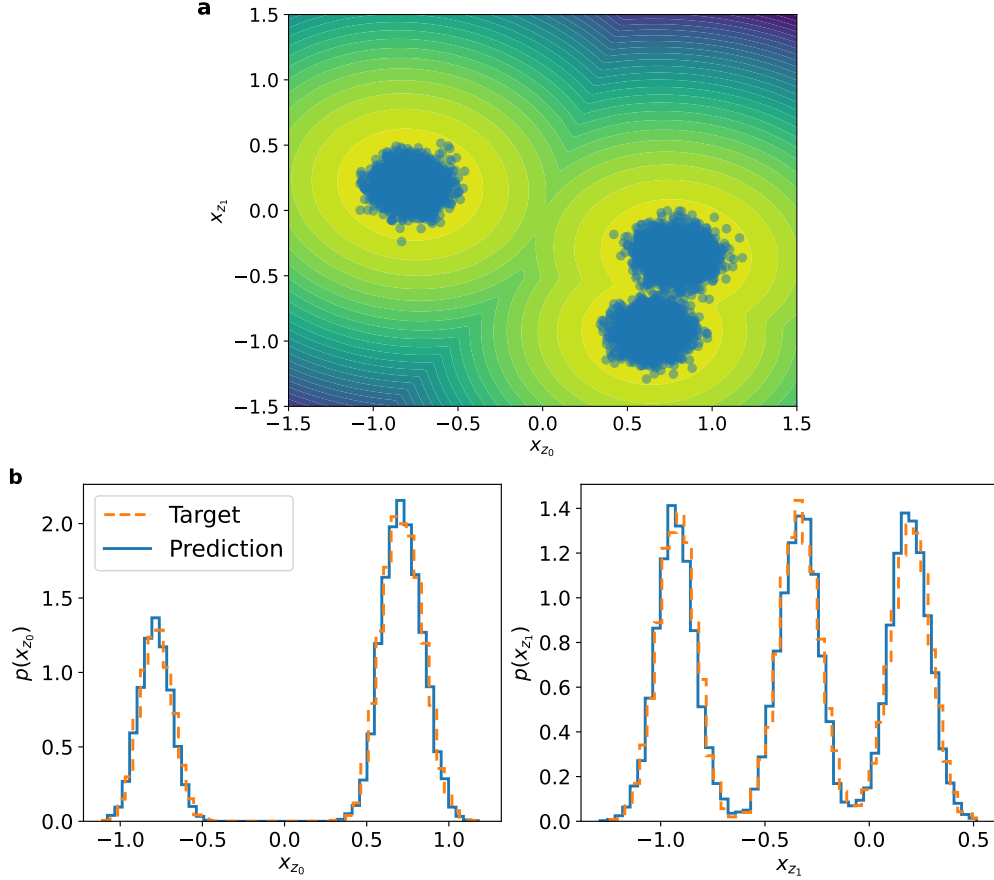


Figure 6: (a) Scatter plot of \mathbf{x}_z -coordinates of independent samples drawn from the learned q_θ . The contour lines correspond to the target, multimodal distribution $p(\mathbf{x}_z)$. (b) One-dimensional marginals of the \mathbf{x}_z -coordinates ($\dim(\mathbf{x}_z) = 2$) as computed from the learned q_θ (blue) vs target $p(\mathbf{x}_z)$ (orange) at $\beta_{\text{target}} = 1$.

In the higher-dimensional case ($\dim(\mathbf{x}) = 20$), it becomes even more important to correctly identify the lower-dimensional subspace where the multimodality is concentrated. As has been reported in other works, we have also found that the mode-seeking behavior of the reverse KL-objective is more pronounced in this higher-dimensional setting. The learned transformation, i.e., the right-stochastic matrix A_ϕ and its inverse, can be seen in Figure 7. We observe that despite initializing with an almost uniform matrix, it converges to one where the new coordinates \mathbf{z} are mostly associated with \mathbf{x}_z , i.e., the original coordinates along which the multimodality is concentrated. This is more obvious in the inverse A_ϕ^{-1} , which exhibits a largely diagonal structure along the aforementioned partitioning.

In Figure 9, some pairs of \mathbf{x}_z -coordinates corresponding to independent samples drawn from the trained model $q_\theta(\mathbf{X}, \mathbf{z})$ and transformation f_ϕ are depicted against contour lines from the corresponding target marginal $p(\mathbf{x}_z)$. On the left side, we show samples obtained after the adaptive tempering scheme proposed has been employed, and on the right side without ($\beta_{\text{target}} = 1$). We observe that the samples obtained without tempering are concentrated on one of the three modes, and the model fails to identify the other two. The application of the adaptive tempering scheme overcomes this mode-seeking behavior. In Figure 8, we compare the learned (with adaptive tempering) one-dimensional marginals for each of the ten \mathbf{x}_z -coordinates against the reference ones. We observe that the proposed model is capable of accurately capturing all modes along all ten dimensions.

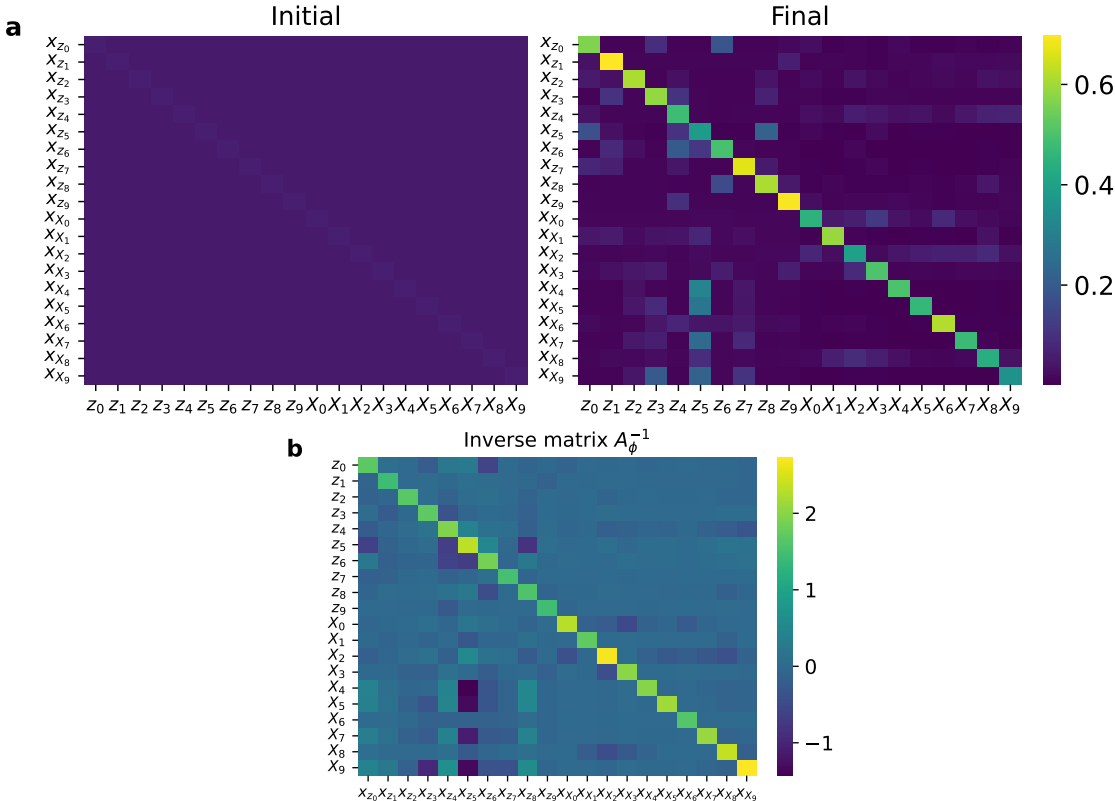


Figure 7: (a) Right stochastic matrix A_ϕ of the 20 dimensional \mathbf{x} -coordinates at (left) initialization and (right) at target inverse temperature $\beta = 1$. (b) Inverse matrix A_ϕ^{-1} at $\beta = 1$.

3.3 Alanine Dipeptide

The following section focuses on the data-free coarse-graining of the alanine dipeptide in an implicit solvent, a standard benchmark system with well-characterized collective variables: the dihedral angles (Φ, Ψ) (Figure 10). As the reference, all-atom configuration \mathbf{x} , against which all subsequent comparisons are performed, we choose an already coarse-grained version of the alanine dipeptide, where the hydrogen atoms have been removed. The employed potential energy function $U(\mathbf{x})$ is represented by the Graph Neural Network DimeNet [91] which was trained with the relative entropy method [25].

The reference molecule consists of 10 atoms. We remove rigid body motions by fixing 6 of the total 30 Cartesian coordinates, resulting in $\dim(\mathbf{x}) = 30 - 6 = 24$. In particular, we fix atom 4 at the origin $(0, 0, 0)$, atom 5 along the 3rd-axis at $(0, 0, x_3^{(5)})$, and atom 7 on the 1–3-plane at $(x_1^{(7)}, 0, x_1^{(7)})$ as shown in Figure 10 [66]. This has proven effective, particularly given the wide range of temperatures at which we train. Additionally, we fix the coordinate $x_3^{(5)}$ of the nitrogen atom 5 to always be on the negative side in order to suppress mirror images that arise by simply flipping the direction of the bond. We note that the aforementioned potential cannot differentiate between the two mirror images found in alanine (L-form and D-form). Since we exclusively see the L-form in nature [92, 93], we add a harmonic term [29] to penalize configurations corresponding to the D-form.

The target temperature is $T = 330$ K (corresponding to $\beta_{\text{target}} = 1$). We generated reference data by running 24 parallel chains using the NUTS sampler, resulting in a total of 2.4×10^6 steps. To improve statistical accuracy and expedite convergence, the chains were initialized at carefully selected configurations located within free-energy wells defined by dihedral angles Φ and Ψ . Random initialization would require prohibitively long simulations to populate all relevant configurational regions with the correct statistical weight, even for a small molecule such as alanine dipeptide. Despite this guided initialization, the overall cost of generating the reference data was approximately $\mathcal{O}(10^9)$ energy evaluations.

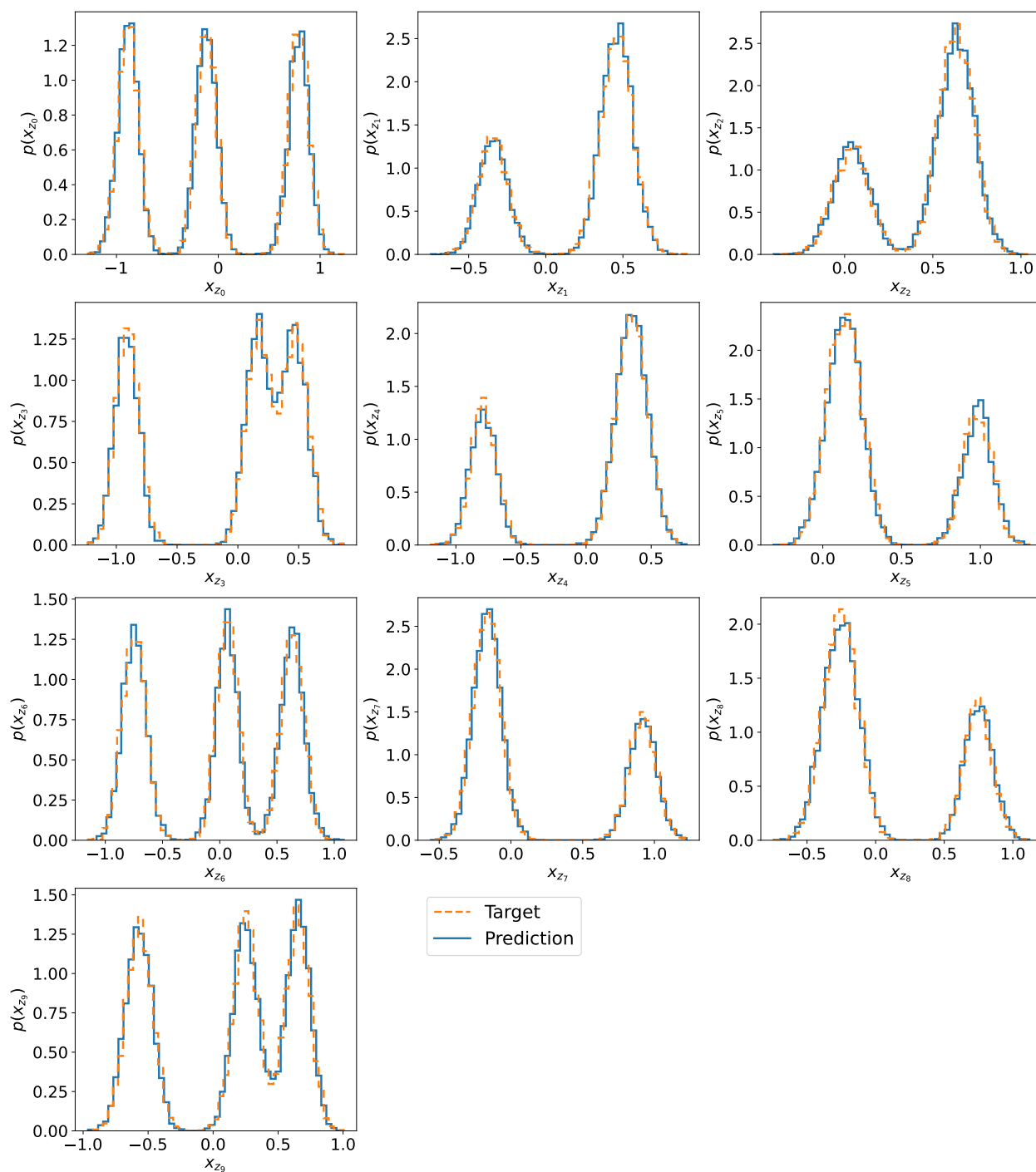


Figure 8: One-dimensional marginals of the \mathbf{x}_z -coordinates ($\dim(\mathbf{x}_z) = 10$) as computed from the learned q_θ (blue) vs target $p(\mathbf{x}_z)$ (orange) at $\beta_{\text{target}} = 1$.

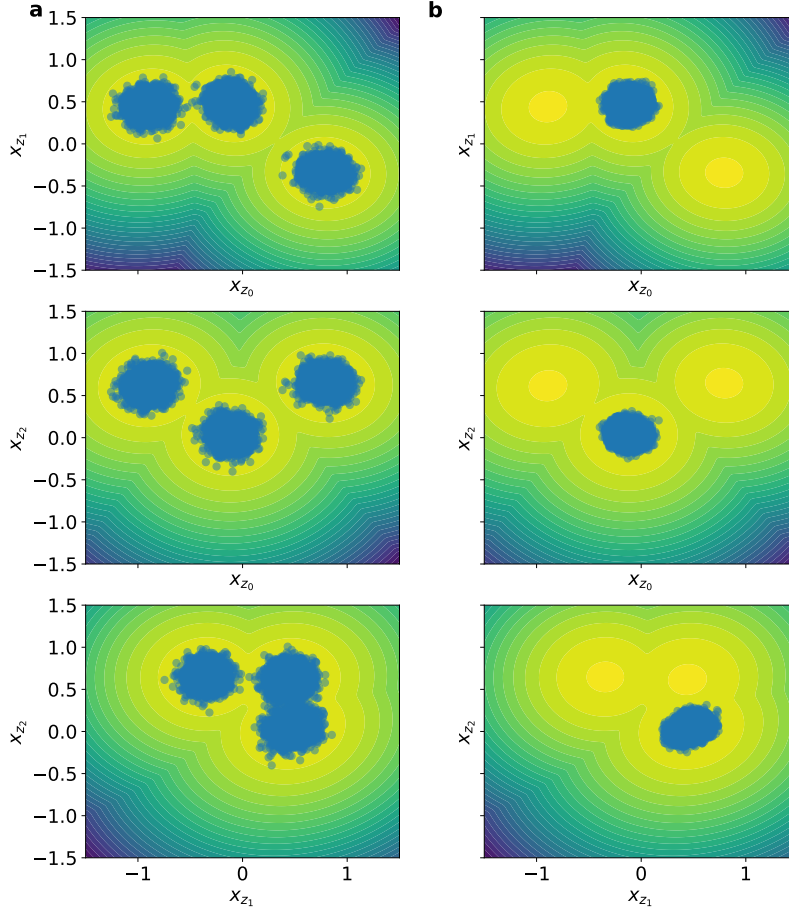


Figure 9: Scatter plots of different pairs of the 10-dimensional coordinates \mathbf{x}_z drawn from $q_\theta(\mathbf{z})$. The contour lines correspond to the target multimodal distribution $p(\mathbf{x}_z)$ ($\beta_{\text{target}} = 1$). (a) With tempering, and (b) without tempering. One observes that the latter leads to several modes of the target not being represented in $q_\theta(\mathbf{z})$.

Table 5: Normalizing Flow Architecture for g_θ (see Equation (7)) in the Alanine Dipeptide Example.

Coupling layers	MLP layers	MLP width	RQS knots	RQS Interval	$\dim(\theta)$
8	4	64	8	$[-4, 4]$	224576

In contrast, the training of the proposed method does *not* rely on such initialization strategies. Our model requires approximately $\mathcal{O}(10^7)$ energy evaluations per tempering step, and about $\mathcal{O}(10^9)$ in total. While the total computational cost in terms of energy evaluations is comparable to that of generating the reference data, we emphasize two key advantages: (i) our training does not exploit preselected starting configurations, and (ii) the trained model produces a fully predictive generative representation capable of generating independent, one-shot equilibrium samples across all temperature steps.

The proposed formulation utilizes a normalizing flow model for $g_\theta(\epsilon)$, as described in Table 5. The parameters for the conditional distribution $q_\theta(\mathbf{X}|\mathbf{z})$ can be found in Table 6. We emphasize that the proposed model has approximately **one order of magnitude fewer parameters** compared to similar normalizing flow models that have been previously employed for (roughly) the same alanine dipeptide molecule [54]. We optimize the parameters θ using the ADAM optimizer with a learning rate of $\eta_{\text{SGD}} = 5.0 \times 10^{-4}$. We skip updates with very large gradients, and clip moderate gradients according to the scheme in Midgley et al.. We track the gradient norm of the last 50 updates and skip gradient steps, where the norm is 10 times higher than the median, and clip gradients, where the gradient norm is 5 times higher than the median. This improves training stability, especially early on, when the flow model provides a very poor approximation of the target.

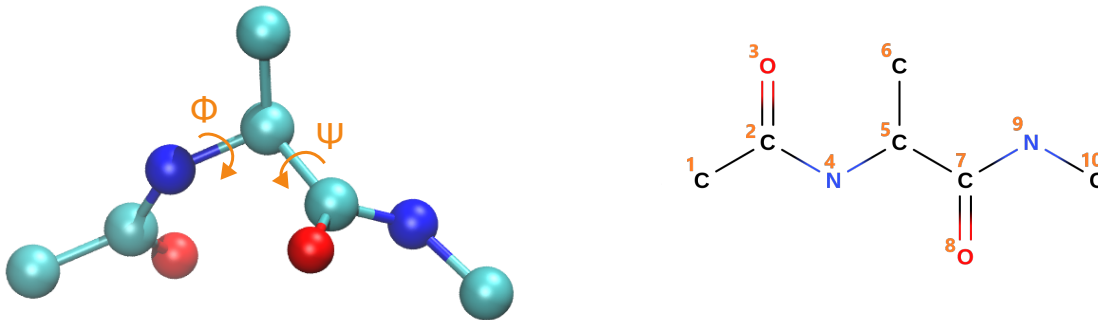


Figure 10: Dihedral angles (Φ , Ψ) for coarse-grained alanine dipeptide (left) and atom numbering in the CG alanine dipeptide (right). We fix atom 4 at the origin $(0, 0, 0)$, atom 5 along the 3rd-axis at $(0, 0, x_3^{(5)})$, and atom 7 on the 1–3-plane at $(x_1^{(7)}, 0, x_1^{(7)})$ in order to remove rigid body motions.

Table 6: MLP Architecture Used for Mean and Variance of $q_\theta(\mathbf{X}|\mathbf{z})$ (see Equation (13)).

MLP layers	MLP width	Activation layer	dim(θ)
8	90	ReLU	60408

Convergence at the initial $\beta_0 = 0.0001$ is crucial and for this reason we employ $L = 15000$ update steps and take $N = 10000$ samples to estimate the gradients. For the adaptive tempering, we use $\delta KL_{\max} = 0.1$, $\Delta\beta_{\max} = 0.005$ (see Algorithm 1). Once the flow is trained at the initial temperature, we train for $L = 1000$ update steps per tempering step until we reach the target $\beta_{\text{target}} = 1$.

In our experiments, we set $\dim(\mathbf{z}) = 15$ and $\dim(\mathbf{X}) = 9$, corresponding to 5 and 3 pseudoatoms, respectively. Figure 11 visualizes the learned transformation based on \mathbf{A}_ϕ^{-1} . The color intensity indicates the contribution strength of each real atom $\mathbf{x}_{(i)}$ to the corresponding pseudoatom $\mathbf{z}_{(j)}$. We observe that the learned pseudoatoms predominantly align with the backbone atoms and also capture the contributions of the oxygen atoms. Finally, we note that the first nitrogen atom is fixed at the origin, as previously described, and is therefore excluded from the transformation.

In order to provide further insight on the identified CG coordinates \mathbf{z} , we explore their correlation with the dihedral angles (Φ , Ψ) in Figure 14. For each bin in the Ramachandran plot, we average the value of each individual CG-coordinate \mathbf{z}_j inside that bin. This gives us an indication of the expected value of \mathbf{z}_j given a pair (Φ , Ψ). The color indicates the average latent variable activation for all conformations in that region. We select four coordinates to highlight different correlations between coordinates and dihedral angles.

We assess the predictive accuracy of the proposed model in terms of various observables. Firstly, results in terms of Ramachandran plots and various inverse temperatures can be seen in Figure 12. For the target temperature, we also show the one-dimensional marginals of each of the dihedral angles in Figure 13. We note that the proposed model approximates the density $q_\theta(\mathbf{z})$ of the CG coordinates \mathbf{z} and not of the dihedral angles depicted therein. The plots were produced using samples from the learned $q_\theta(\mathbf{X}, \mathbf{z})$. We observe that our method is capable of finding all the relevant modes at all intermediate temperatures. We note that no pre-sampling of the target Boltzmann nor any other prior information on the location of these modes has been employed.

We also provide histograms for the bond distances and angles of the atoms in the system in Figures 15 and 16. These are in very good agreement with the reference structure.

Furthermore, we compute equilibrium distributions of three physical observables: the radius of gyration, the root-mean-squared deviation (RMSD) [94], and the energy U at the target inverse temperature $\beta = 1$. The radius of gyration a_{Rg} for a system of N atoms is given by

$$a_{\text{Rg}}(\mathbf{x}) = \sqrt{\frac{\sum_i^N m_i \|\mathbf{x}_i - \mathbf{x}_{\text{COM}}\|^2}{\sum_i^N m_i}}, \quad (29)$$

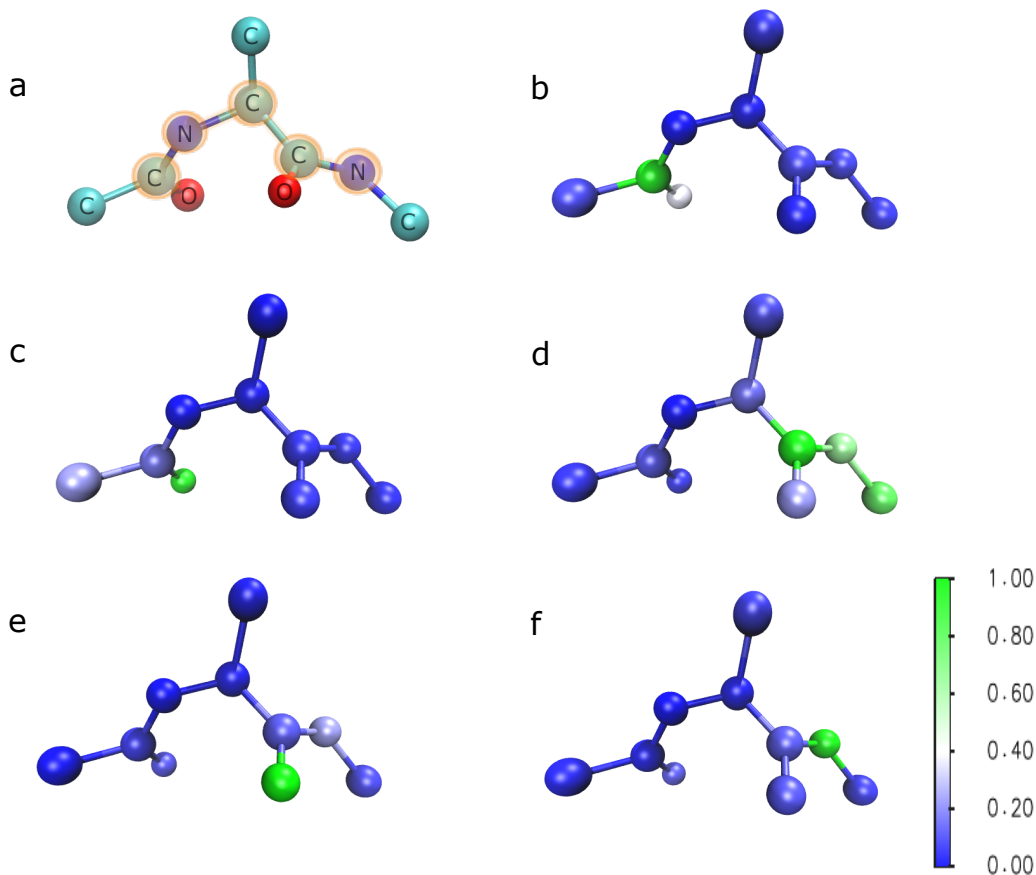


Figure 11: Visualization of associations of pseudoatoms $\mathbf{z}_{(j)}$ with actual atoms $\mathbf{x}_{(i)}$ based on the learned inverse of \mathbf{A}_{ϕ}^{-1} . The first configuration (a) is selected from the reference simulation for comparison. The backbone atoms, responsible for the dihedral angles (Φ, Ψ) , are highlighted in orange. The second configuration is sampled from q_{θ} and colored based on \mathbf{A}_{ϕ}^{-1} for pseudoatom (b) $\mathbf{z}_{(0)}$, (c) $\mathbf{z}_{(1)}$, (d) $\mathbf{z}_{(2)}$, (e) $\mathbf{z}_{(3)}$, and (f) $\mathbf{z}_{(4)}$. One observes that the \mathbf{z} -coordinates are associated with the backbone atoms and oxygen atoms of the dipeptide.

where m_i is the mass of each atom i with Cartesian coordinates \mathbf{x}_i . The center of mass (COM) is computed as $\mathbf{x}_{\text{COM}} = \frac{\sum_i^N m_i \mathbf{x}_i}{\sum_i^N m_i}$. The root-mean-squared deviation a_{RMSD} is calculated with respect to a reference configuration \mathbf{x}_{ref} , which in this study was assumed to be a randomly selected position of the reference trajectory, as

$$a_{\text{RMSD}}(\mathbf{x}, \mathbf{x}_{\text{ref}}) = \sqrt{\frac{1}{N} \sum_i^N |\mathbf{x}_i - \mathbf{x}_{\text{ref}}|^2} \quad (30)$$

The histograms of these observables in Figure 17 are computed using 5000 samples from the trained model generated as described in Section 2.3. The results for all three observables show excellent agreement with those obtained from the reference simulation.

Finally, we evaluate the quality of the generated structures by computing two scores: the bond score and the diversity score [15]. The bond score calculates how many bonded atom distances lie within 10 % of the bond distance in the reference trajectory. The diversity score compares the average RMSD between generated structures themselves with the RMSD between generated structures and the atomistic reference [14, 15]. The score lies in the $[0, 1]$ range. A score close to zero indicates the generated distribution is both diverse and faithful to the reference ensemble. The scores in Table 7 have been obtained by averaging over 10 trajectories of generated samples.

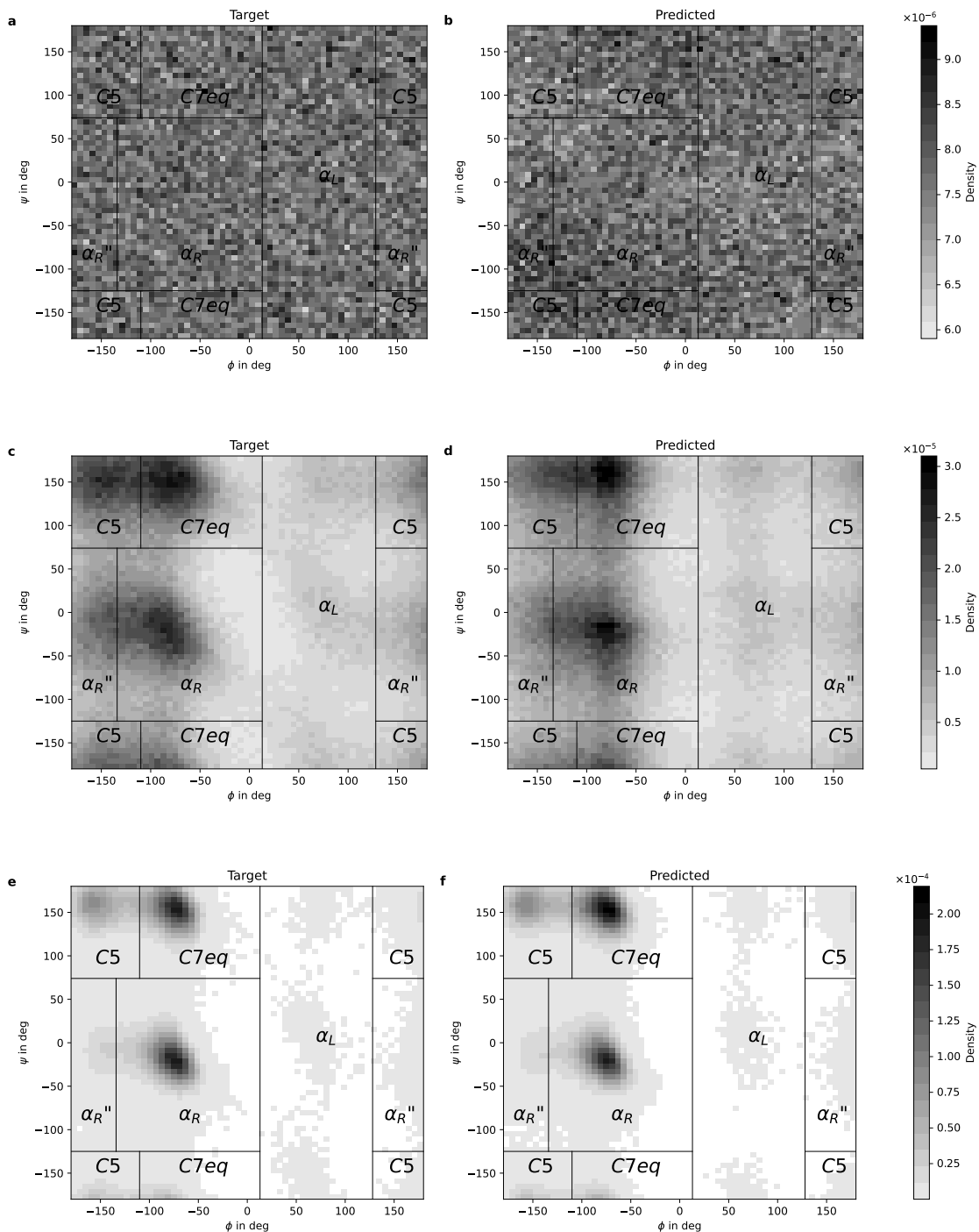


Figure 12: Ramachandran plots of the (Φ, Ψ) dihedral angle distributions obtained from the reference simulations (left) and predicted by the proposed method (right) at different inverse temperatures. Panels (a, b) correspond to $\beta \approx 0$, panels (c, d) correspond to $\beta \approx 0.22$, and panels (e, f) correspond to $\beta = 1$.

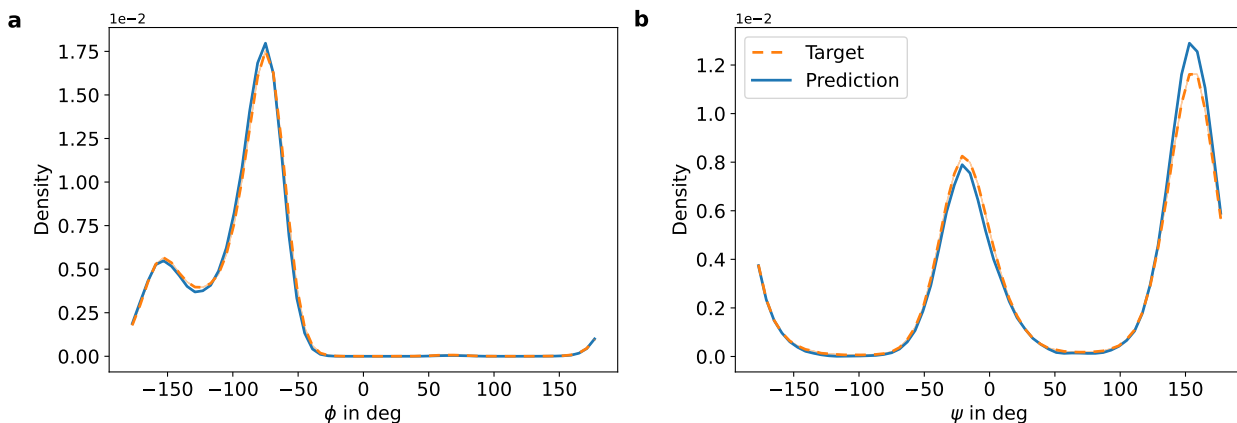


Figure 13: Comparison of the dihedral density of (a) Φ and (b) Ψ obtained from simulations of the all-atom Boltzmann density (orange) and the proposed method (blue).

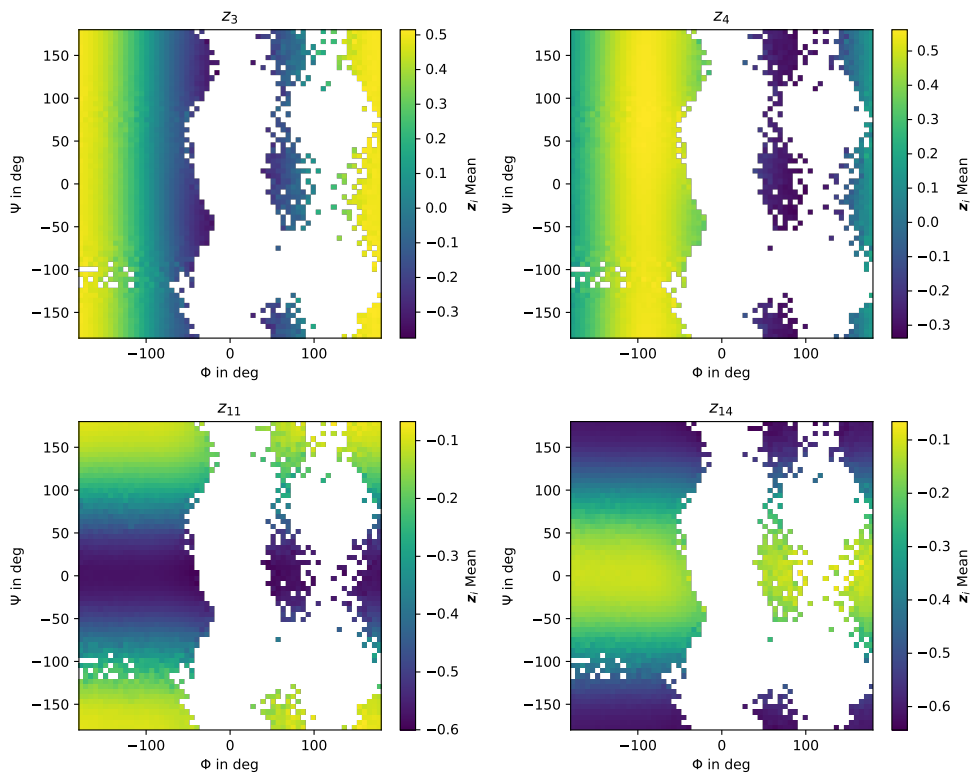


Figure 14: Ramachandran plots of the predicted (Φ , Ψ) dihedral angle distributions. We color each bin in the histogram based on the average value of all individual CG coordinates z_j inside that bin. Titles indicate the z_j component. (Top left): z_3 , (top right) z_4 , (bottom left) z_{11} , and (bottom right) z_{14} .

Table 7: Bond and Diversity scores. Standard deviations are obtained by averaging the results for 10 trajectories of generated samples.

bond score (\uparrow) [%]	diversity score (\downarrow)
0.99848 ± 0.00001	0.0106 ± 0.0055

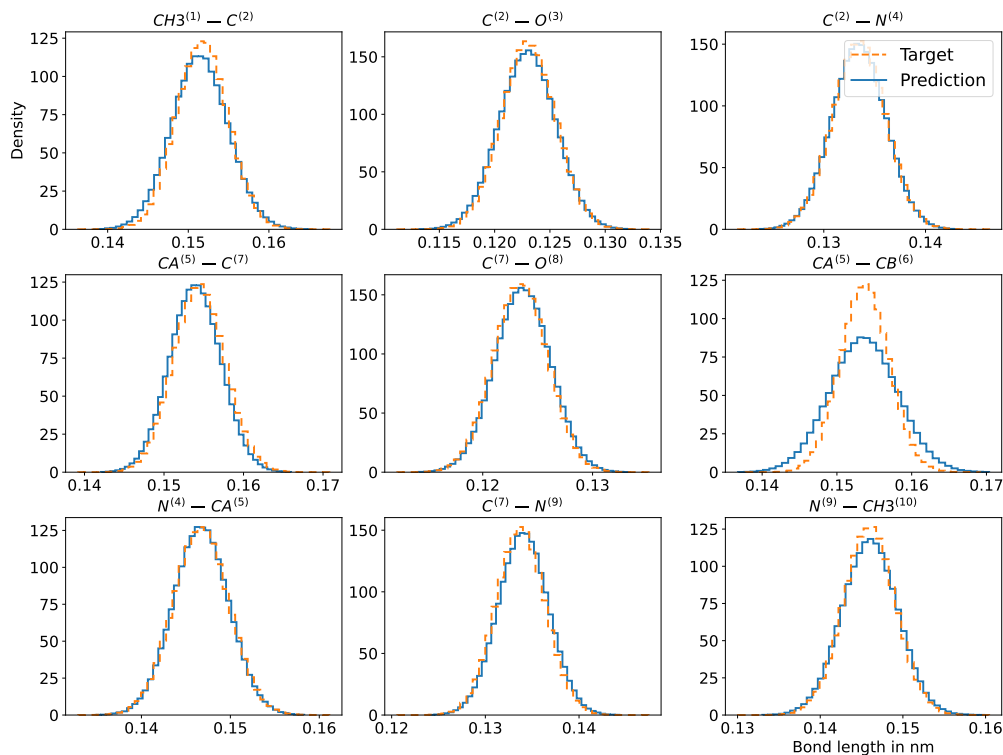


Figure 15: Comparison of various bond-length histograms (in nm) obtained from simulations using the all-atom Boltzmann density (orange) and the proposed method (blue).

4 Conclusions

We have presented a fully data-free, generative framework for coarse-graining that approximates the full atomistic Boltzmann distribution using only evaluations of the interatomic potential and forces. The model is trained by minimizing the reverse Kullback-Leibler divergence, and to overcome its well-known mode-seeking behavior, we introduce a novel adaptive tempering scheme based on information-theoretic criteria. Our approach unifies the two central objectives of coarse-graining—learning a coarse-graining transformation and fitting a generative probabilistic model—into a single learning problem, by training a bijective map from a structured latent space to full atomistic configurations. The latent space separates slow, coarse-grained variables, which capture multimodal metastable states, from fast variables representing local thermal fluctuations, enabling an accurate, one-shot reconstruction of all-atom structures.

We demonstrated the proposed approach for benchmark problems, including a double-well potential, a Gaussian mixture model, and the alanine dipeptide molecule. Our experiments show that the method can successfully capture highly multimodal target distributions without missing modes, even in regimes where reverse KL-based training is known to fail. The adaptive tempering scheme, although it introduces computational overhead, provides an efficient and automated strategy to reduce the overall training cost.

This framework ensures thermodynamic consistency and automatically identifies physically meaningful coarse-grained variables. By avoiding reliance on precollected MD trajectories, the method eliminates the bottleneck of costly or incomplete data generation, addressing the “chicken-and-egg” problem in coarse-graining.

Although this study employed relatively lightweight neural network architectures, the framework can be extended to more expressive models, such as equivariant normalizing flows [45, 95] or graph neural networks [83, 96], to further improve accuracy and generalization. Overall, our results establish a scalable, interpretable, and thermodynamically faithful approach to data-free coarse-graining, providing a unified, principled solution to both sampling and back-mapping challenges in molecular modeling.

In the future, we intend to extend the proposed framework to more complex molecular systems.

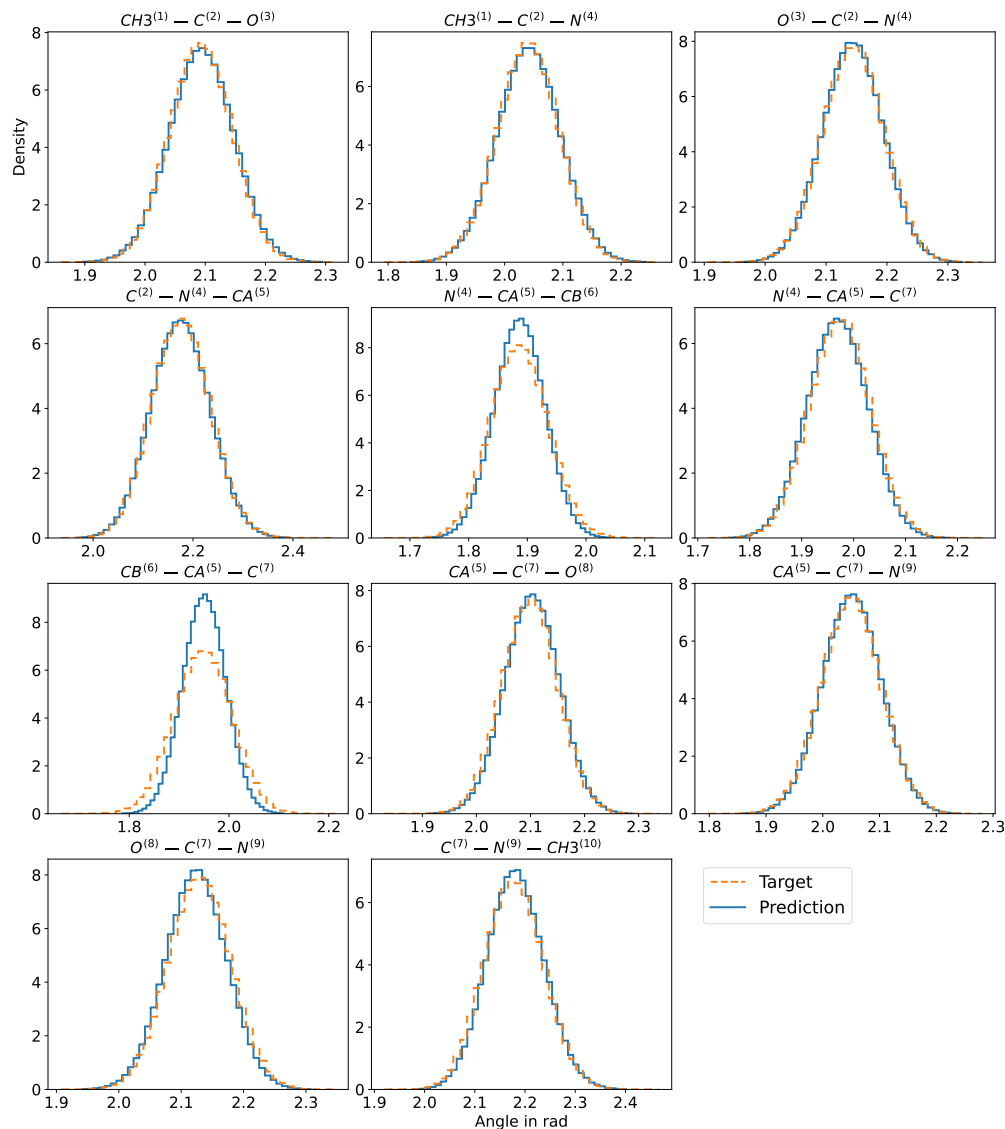


Figure 16: Comparison of various bond-angle histograms (in rad) obtained from simulations using the all-atom Boltzmann density (orange) and the proposed method (blue).

In this work, we restricted our attention to the special case, where f_ϕ , introduced in Equation (2), is a learnable linear transformation. This choice provides more interpretable mappings and can be readily made equivariant with respect to rigid-body motions; several promising research directions remain open. Extending the analysis to nonlinear transformations (e.g., with the use of another invertible, normalizing flow model) could uncover more powerful coarse-grained representations that yield clearer separations and enable more accurate approximations.

Regardless of whether a linear or nonlinear map is used, the dimension of the CG space, $\dim(\mathbf{z})$, must still be prescribed by the user. While the objective, i.e., the KL-divergence in Equation (9), naturally provides a score function for comparing models with different $\dim(\mathbf{z})$, it would be highly beneficial to develop an *adaptive scheme* that can automatically adjust the dimensionality, ideally starting from small values and progressively increasing $\dim(\mathbf{z})$ until no further improvements in the objective are observed. Finally, we note that although the proposed adaptive tempering scheme substantially mitigates the well-known pathologies of the reverse KL-divergence in energy-based training, it does not rule out the possibility that alternative optimization objectives (such as the Fisher or χ^2 divergences discussed above) could offer a more stable and computationally efficient learning procedure.

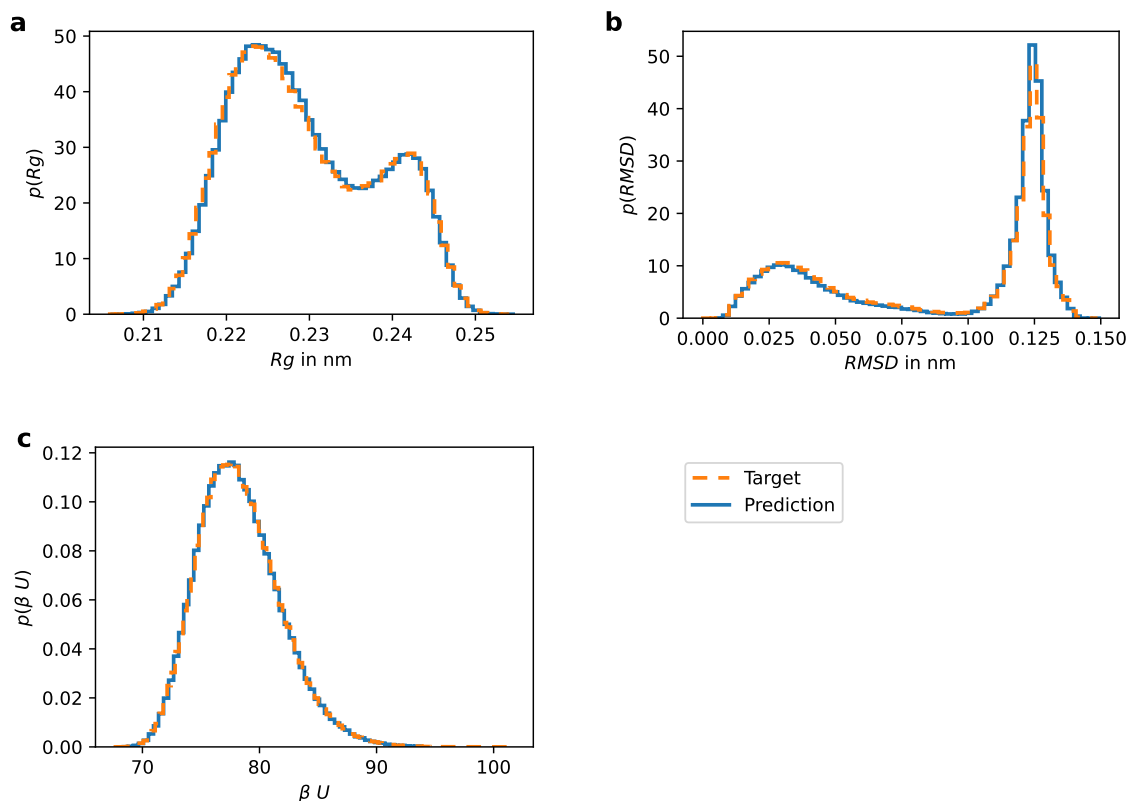


Figure 17: Comparison of histograms for the following observables obtained from simulations of the all-atom Boltzmann density (orange) and the proposed method (blue). (a) Radius of gyration. (b) Root-mean-squared deviation. (c) Energy at the target temperature.

Acknowledgement

This work was funded by the Excellence Strategy of the Federal Government and the Länder in the context of the ARTEMIS Innovation Network.

References

- [1] B. J. Alder and T. E. Wainwright. Studies in Molecular Dynamics. I. General Method. *The Journal of Chemical Physics*, 31(2):459–466, 08 2004. ISSN 0021-9606. doi:10.1063/1.1730376. URL <https://doi.org/10.1063/1.1730376>.
- [2] Nicholas Metropolis and S. Ulam. The Monte Carlo Method. *Journal of the American Statistical Association*, 44 (247):335–341, September 1949. ISSN 0162-1459. doi:10.1080/01621459.1949.10483310. URL <https://www.tandfonline.com/doi/abs/10.1080/01621459.1949.10483310>. Publisher: Taylor & Francis _eprint: <https://www.tandfonline.com/doi/pdf/10.1080/01621459.1949.10483310>.
- [3] Gregory A. Voth. *Coarse-Graining of Condensed Phase and Biomolecular Systems*. Taylor & Francis Inc, London, illustrated edition, September 2008. ISBN 978-1-4200-5955-7.
- [4] W. G. Noid. Perspective: Coarse-grained models for biomolecular systems. *The Journal of Chemical Physics*, 139 (9):090901, September 2013. ISSN 0021-9606. doi:10.1063/1.4818908. URL <https://doi.org/10.1063/1.4818908>.
- [5] Jaehyeok Jin, Alexander J. Pak, Aleksander E. P. Durumeric, Timothy D. Loose, and Gregory A. Voth. Bottom-up Coarse-Graining: Principles and Perspectives. *Journal of Chemical Theory and Computation*, September 2022. ISSN 1549-9618. doi:10.1021/acs.jctc.2c00643. URL <https://doi.org/10.1021/acs.jctc.2c00643>. Publisher: American Chemical Society.

- [6] Evangelia Kalligiannaki, Vagelis Harmandaris, Markos A. Katsoulakis, and Petr Plecháč. The geometry of generalized force matching and related information metrics in coarse-graining of molecular systems. *The Journal of Chemical Physics*, 143(8):084105, August 2015. ISSN 1089-7690. doi:10.1063/1.4928857.
- [7] Markos A. Katsoulakis and José Trashorras. Information Loss in Coarse-Graining of Stochastic Particle Dynamics. *Journal of Statistical Physics*, 122(1):115–135, January 2006. ISSN 1572-9613. doi:10.1007/s10955-005-8063-1. URL <https://doi.org/10.1007/s10955-005-8063-1>.
- [8] Thomas T. Foley, M. Scott Shell, and W. G. Noid. The impact of resolution upon entropy and information in coarse-grained models. *The Journal of Chemical Physics*, 143(24):243104, December 2015. ISSN 1089-7690. doi:10.1063/1.4929836.
- [9] Li-Jun Chen, Hu-Jun Qian, Zhong-Yuan Lu, Ze-Sheng Li, and Chia-Chung Sun. An automatic coarse-graining and fine-graining simulation method: application on polyethylene. *The Journal of Physical Chemistry. B*, 110(47):24093–24100, November 2006. ISSN 1520-6106. doi:10.1021/jp0644558.
- [10] Leandro E. Lombardi, Marcelo A. Martí, and Luciana Capece. CG2AA: backmapping protein coarse-grained structures. *Bioinformatics (Oxford, England)*, 32(8):1235–1237, April 2016. ISSN 1367-4811. doi:10.1093/bioinformatics/btv740.
- [11] Matías R. Machado and Sergio Pantano. SIRAH tools: mapping, backmapping and visualization of coarse-grained models. *Bioinformatics*, 32(10):1568–1570, May 2016. ISSN 1367-4803. doi:10.1093/bioinformatics/btw020. URL <https://doi.org/10.1093/bioinformatics/btw020>.
- [12] Markus Schöberl, Nicholas Zabarar, and Phaedon-Stelios Koutsourelakis. Predictive coarse-graining. *Journal of Computational Physics*, 333:49–77, March 2017. ISSN 0021-9991. doi:10.1016/j.jcp.2016.10.073. URL <http://dx.doi.org/10.1016/j.jcp.2016.10.073>.
- [13] Junhui Peng, Chuang Yuan, Rongsheng Ma, and Zhiyong Zhang. Backmapping from Multiresolution Coarse-Grained Models to Atomic Structures of Large Biomolecules by Restrained Molecular Dynamics Simulations Using Bayesian Inference. *Journal of Chemical Theory and Computation*, 15(5):3344–3353, May 2019. ISSN 1549-9626. doi:10.1021/acs.jctc.9b00062.
- [14] Wujie Wang, Minkai Xu, Chen Cai, Benjamin Kurt Miller, Tess Smidt, Yusu Wang, Jian Tang, and Rafael Gómez-Bombarelli. Generative Coarse-Graining of Molecular Conformations. *arXiv:2201.12176 [physics]*, January 2022. URL <http://arxiv.org/abs/2201.12176>. arXiv: 2201.12176.
- [15] Michael S. Jones, Kirill Shmilovich, and Andrew L. Ferguson. DiAMoNDBack: Diffusion-Denoising Autoregressive Model for Non-Deterministic Backmapping of $C\alpha$ Protein Traces. *Journal of Chemical Theory and Computation*, 19(21):7908–7923, November 2023. ISSN 1549-9618. doi:10.1021/acs.jctc.3c00840. URL <https://doi.org/10.1021/acs.jctc.3c00840>. Publisher: American Chemical Society.
- [16] W. G. Noid, Jih-Wei Chu, Gary S. Ayton, Vinod Krishna, Sergei Izvekov, Gregory A. Voth, Avisek Das, and Hans C. Andersen. The multiscale coarse-graining method. I. A rigorous bridge between atomistic and coarse-grained models. *The Journal of Chemical Physics*, 128(24):244114, June 2008. ISSN 0021-9606. doi:10.1063/1.2938860. URL <https://doi.org/10.1063/1.2938860>.
- [17] W. Tschöp, K. Kremer, O. Hahn, J. Batoulis, and T. Bürger. Simulation of polymer melts. i. coarse-graining procedure for polycarbonates. *Acta Polymerica*, 49(2-3):61 – 74, 1998. doi:10.1002/(sici)1521-4044(199802)49:2/3<61::aid-apol61>3.0.co;2-v. URL <https://www.scopus.com/inward/record.uri?eid=2-s2.0-0032003667&doi=10.1002/2f%28sici%291521-4044%28199802%2949%3a2%2f3%3c61%3a%3aaaid-apol61%3e3.0.co%3b2-v&partnerID=40&md5=8626a3fc36e90aa347df2fae47d59289>.
- [18] Dirk Reith, Mathias Pütz, and Florian Müller-Plathe. Deriving effective mesoscale potentials from atomistic simulations. *Journal of Computational Chemistry*, 24(13):1624–1636, 2003. doi:<https://doi.org/10.1002/jcc.10307>. URL <https://onlinelibrary.wiley.com/doi/abs/10.1002/jcc.10307>.
- [19] Alexander P. Lyubartsev and Aatto Laaksonen. Calculation of effective interaction potentials from radial distribution functions: A reverse monte carlo approach. *Physical Review E*, 52(4):3730 – 3737, 1995. doi:10.1103/PhysRevE.52.3730. URL <https://www.scopus.com/inward/record.uri?eid=2-s2.0-33645078713&doi=10.1103%2fPhysRevE.52.3730&partnerID=40&md5=054fc33f799de10cdf064e923cb479a8>.
- [20] Sergei Izvekov and Gregory A. Voth. Multiscale coarse graining of liquid-state systems. *The Journal of Chemical Physics*, 123(13):134105, 10 2005. ISSN 0021-9606. doi:10.1063/1.2038787. URL <https://doi.org/10.1063/1.2038787>.
- [21] M. Scott Shell. The relative entropy is fundamental to multiscale and inverse thermodynamic problems. *The Journal of Chemical Physics*, 129(14):144108, October 2008. ISSN 0021-9606. doi:10.1063/1.2992060. URL <https://doi.org/10.1063/1.2992060>.

- [22] Linfeng Zhang, Jiequn Han, Han Wang, Roberto Car, and Weinan E. Deepcg: Constructing coarse-grained models via deep neural networks. *The Journal of Chemical Physics*, 149(3):034101, 07 2018. ISSN 0021-9606. doi:10.1063/1.5027645. URL <https://doi.org/10.1063/1.5027645>.
- [23] Jiang Wang, Simon Olsson, Christoph Wehmeyer, Adria Perez, Nicholas E. Charron, Gianni de Fabritiis, Frank Noe, and Cecilia Clementi. Machine Learning of coarse-grained Molecular Dynamics Force Fields, April 2019. URL <http://arxiv.org/abs/1812.01736>. arXiv:1812.01736 [physics, stat].
- [24] Brooke E. Husic, Nicholas E. Charron, Dominik Lemm, Jiang Wang, Adria Pérez, Andreas Krämer, Yaoyi Chen, Simon Olsson, Gianni de Fabritiis, Frank Noé, and Cecilia Clementi. Coarse Graining Molecular Dynamics with Graph Neural Networks. *arXiv:2007.11412 [physics, q-bio, stat]*, August 2020. URL <http://arxiv.org/abs/2007.11412>.
- [25] Stephan Thaler, Maximilian Stupp, and Julija Zavadlav. Deep coarse-grained potentials via relative entropy minimization. *The Journal of Chemical Physics*, 157(24):244103, December 2022. ISSN 0021-9606. doi:10.1063/5.0124538. URL <https://doi.org/10.1063/5.0124538>.
- [26] Jonas Köhler, Yaoyi Chen, Andreas Krämer, Cecilia Clementi, and Frank Noé. Flow-Matching: Efficient Coarse-Graining of Molecular Dynamics without Forces. *Journal of Chemical Theory and Computation*, 19(3):942–952, February 2023. ISSN 1549-9618. doi:10.1021/acs.jctc.3c00016. URL <https://doi.org/10.1021/acs.jctc.3c00016>. Publisher: American Chemical Society.
- [27] Diederik P. Kingma and Max Welling. Auto-Encoding Variational Bayes, December 2013. URL <http://arxiv.org/abs/1312.6114>. arXiv:1312.6114 [cs, stat].
- [28] Ian J. Goodfellow, Jean Pouget-Abadie, Mehdi Mirza, Bing Xu, David Warde-Farley, Sherjil Ozair, Aaron Courville, and Yoshua Bengio. Generative adversarial networks, 2014. URL <https://arxiv.org/abs/1406.2661>.
- [29] Wujie Wang and Rafael Gómez-Bombarelli. Coarse-graining auto-encoders for molecular dynamics. *npj Computational Materials*, 5(1):1–9, December 2019. ISSN 2057-3960. doi:10.1038/s41524-019-0261-5. URL <https://www.nature.com/articles/s41524-019-0261-5>.
- [30] Wei Li, Craig Burkhardt, Patrycja Polińska, Vagelis Harmandaris, and Manolis Doxastakis. Backmapping coarse-grained macromolecules: An efficient and versatile machine learning approach. *The Journal of Chemical Physics*, 153(4):041101, 07 2020. ISSN 0021-9606. doi:10.1063/5.0012320. URL <https://doi.org/10.1063/5.0012320>.
- [31] Marc Stieffenhofer, Michael Wand, and Tristan Bereau. Adversarial reverse mapping of equilibrated condensed-phase molecular structures, 2020. URL <https://arxiv.org/abs/2003.07753>.
- [32] Marc Stieffenhofer, Tristan Bereau, and Michael Wand. Adversarial reverse mapping of condensed-phase molecular structures: Chemical transferability. *APL Materials*, 9(3):031107, 03 2021. ISSN 2166-532X. doi:10.1063/5.0039102. URL <https://doi.org/10.1063/5.0039102>.
- [33] Mary A. Rohrdanz, Wenwei Zheng, and Cecilia Clementi. Discovering mountain passes via torchlight: Methods for the definition of reaction coordinates and pathways in complex macromolecular reactions. *Annual review of physical chemistry*, 64:295–316, 2013. Publisher: Annual Reviews.
- [34] G. M. Torrie and J. P. Valleau. Nonphysical sampling distributions in Monte Carlo free-energy estimation: Umbrella sampling. *Journal of Computational Physics*, 23(2):187–199, February 1977. ISSN 0021-9991. doi:10.1016/0021-9991(77)90121-8. URL <https://www.sciencedirect.com/science/article/pii/0021999177901218>.
- [35] Marc Souaille and Benoît Roux. Extension to the weighted histogram analysis method: combining umbrella sampling with free energy calculations. *Computer Physics Communications*, 135(1):40–57, March 2001. ISSN 0010-4655. doi:10.1016/S0010-4655(00)00215-0. URL <https://www.sciencedirect.com/science/article/pii/S0010465500002150>.
- [36] Alessandro Barducci, Massimiliano Bonomi, and Michele Parrinello. Metadynamics. *WIREs Computational Molecular Science*, 1(5):826–843, 2011. ISSN 1759-0884. doi:10.1002/wcms.31. URL <https://onlinelibrary.wiley.com/doi/abs/10.1002/wcms.31>. _eprint: <https://onlinelibrary.wiley.com/doi/pdf/10.1002/wcms.31>.
- [37] M. Bonomi, A. Barducci, and M. Parrinello. Reconstructing the equilibrium Boltzmann distribution from well-tempered metadynamics. *Journal of Computational Chemistry*, 30(11):1615–1621, 2009. ISSN 1096-987X. doi:10.1002/jcc.21305. URL <https://onlinelibrary.wiley.com/doi/abs/10.1002/jcc.21305>. _eprint: <https://onlinelibrary.wiley.com/doi/pdf/10.1002/jcc.21305>.

- [38] Alessandro Laio and Michele Parrinello. Escaping free-energy minima. *Proceedings of the National Academy of Sciences*, 99(20):12562–12566, October 2002. doi:10.1073/pnas.202427399. URL <https://www.pnas.org/doi/10.1073/pnas.202427399>. Publisher: Proceedings of the National Academy of Sciences.
- [39] I. Bilonis and P. S. Koutsourelakis. Free energy computations by minimization of Kullback–Leibler divergence: An efficient adaptive biasing potential method for sparse representations. *Journal of Computational Physics*, 231(9):3849–3870, May 2012. ISSN 0021-9991. doi:10.1016/j.jcp.2012.01.033. URL <https://www.sciencedirect.com/science/article/pii/S0021999112000630>.
- [40] Andrew L. Ferguson, Athanassios Z. Panagiotopoulos, Ioannis G. Kevrekidis, and Pablo G. Debenedetti. Nonlinear dimensionality reduction in molecular simulation: The diffusion map approach. *Chemical Physics Letters*, 509(1):1–11, June 2011. ISSN 0009-2614. doi:10.1016/j.cplett.2011.04.066. URL <https://www.sciencedirect.com/science/article/pii/S0009261411004957>.
- [41] Frank Noé, Simon Olsson, Jonas Köhler, and Hao Wu. Boltzmann generators: Sampling equilibrium states of many-body systems with deep learning. *Science*, 365(6457):eaaw1147, September 2019. doi:10.1126/science.aaw1147. URL <https://www.science.org/doi/10.1126/science.aaw1147>. Publisher: American Association for the Advancement of Science.
- [42] George Papamakarios, Eric Nalisnick, Danilo Jimenez Rezende, Shakir Mohamed, and Balaji Lakshminarayanan. Normalizing flows for probabilistic modeling and inference, 2021. URL <https://arxiv.org/abs/1912.02762>.
- [43] Manuel Dibak, Leon Klein, Andreas Krämer, and Frank Noé. Temperature steerable flows and boltzmann generators. *Phys. Rev. Res.*, 4:L042005, Oct 2022. doi:10.1103/PhysRevResearch.4.L042005. URL <https://link.aps.org/doi/10.1103/PhysRevResearch.4.L042005>.
- [44] Maximilian Schebek, Michele Invernizzi, Frank Noé, and Jutta Rogal. Efficient mapping of phase diagrams with conditional boltzmann generators. *Machine Learning: Science and Technology*, 5(4):045045, nov 2024. doi:10.1088/2632-2153/ad849d. URL <https://dx.doi.org/10.1088/2632-2153/ad849d>.
- [45] Jonas Köhler, Leon Klein, and Frank Noe. Equivariant flows: Exact likelihood generative learning for symmetric densities. In Hal Daumé III and Aarti Singh, editors, *Proceedings of the 37th International Conference on Machine Learning*, volume 119 of *Proceedings of Machine Learning Research*, pages 5361–5370. PMLR, 13–18 Jul 2020. URL <https://proceedings.mlr.press/v119/kohler20a.html>.
- [46] Hao Wu, Jonas Köhler, and Frank Noé. Stochastic normalizing flows, 2020. URL <https://arxiv.org/abs/2002.06707>.
- [47] Marylou Gabrié, Grant M. Rotskoff, and Eric Vanden-Eijnden. Adaptive Monte Carlo augmented with normalizing flows. *Proceedings of the National Academy of Sciences*, 119(10):e2109420119, March 2022. doi:10.1073/pnas.2109420119. URL <https://www.pnas.org/doi/full/10.1073/pnas.2109420119>. Publisher: Proceedings of the National Academy of Sciences.
- [48] Sergey Samsonov, Evgeny Lagutin, Marylou Gabrié, Alain Durmus, Alexey Naumov, and Eric Moulines. Local-global mcmc kernels: the best of both worlds. In S. Koyejo, S. Mohamed, A. Agarwal, D. Belgrave, K. Cho, and A. Oh, editors, *Advances in Neural Information Processing Systems*, volume 35, pages 5178–5193. Curran Associates, Inc., 2022. URL https://proceedings.neurips.cc/paper_files/paper/2022/file/21c86d5b10cdc28664ccdadf0a29065a-Paper-Conference.pdf.
- [49] Ana Molina-Taborda, Pilar Cossio, Olga Lopez-Acevedo, and Marylou Gabrié. Active learning of boltzmann samplers and potential energies with quantum mechanical accuracy. *Journal of Chemical Theory and Computation*, 20(20):8833–8843, 2024. doi:10.1021/acs.jctc.4c00506. URL <https://doi.org/10.1021/acs.jctc.4c00506>. PMID: 39370622.
- [50] Peter Wirnsberger, George Papamakarios, Borja Ibarz, Sébastien Racanière, Andrew J Ballard, Alexander Pritzel, and Charles Blundell. Normalizing flows for atomic solids. *Machine Learning: Science and Technology*, 3(2):025009, June 2022. ISSN 2632-2153. doi:10.1088/2632-2153/ac6b16. URL <https://iopscience.iop.org/article/10.1088/2632-2153/ac6b16>.
- [51] Vincent Stimper, Bernhard Schölkopf, and José Miguel Hernández-Lobato. Resampling base distributions of normalizing flows, 2022. URL <https://arxiv.org/abs/2110.15828>.
- [52] Loris Felardos, Jérôme Hénin, and Guillaume Charpiat. Designing losses for data-free training of normalizing flows on Boltzmann distributions, January 2023. URL <http://arxiv.org/abs/2301.05475>. arXiv:2301.05475 [cond-mat].
- [53] Loris Felardos, Jérôme Hénin, and Guillaume Charpiat. Designing losses for data-free training of normalizing flows on boltzmann distributions, 2023. URL <https://arxiv.org/abs/2301.05475>.

- [54] Laurence Illing Midgley, Vincent Stimper, Gregor N. C. Simm, Bernhard Schölkopf, and José Miguel Hernández-Lobato. Flow Annealed Importance Sampling Bootstrap, March 2023. URL <http://arxiv.org/abs/2208.01893>. arXiv:2208.01893 [cs, q-bio, stat].
- [55] Laurence I. Midgley, Vincent Stimper, Javier Antorán, Emile Mathieu, Bernhard Schölkopf, and José Miguel Hernández-Lobato. Se(3) equivariant augmented coupling flows, 2024. URL <https://arxiv.org/abs/2308.10364>.
- [56] Qinsheng Zhang and Yongxin Chen. Path Integral Sampler: a stochastic control approach for sampling, March 2022. URL <http://arxiv.org/abs/2111.15141>. arXiv:2111.15141 [cs].
- [57] Francisco Vargas, Will Grathwohl, and Arnaud Doucet. Denoising Diffusion Samplers, August 2023. URL <http://arxiv.org/abs/2302.13834>. arXiv:2302.13834 [cs].
- [58] Julius Berner, Lorenz Richter, and Karen Ullrich. An optimal control perspective on diffusion-based generative modeling, March 2024. URL <http://arxiv.org/abs/2211.01364>. arXiv:2211.01364 [cs].
- [59] Tara Akhound-Sadegh, Jarrid Rector-Brooks, Avishek Joey Bose, Sarthak Mittal, Pablo Lemos, Cheng-Hao Liu, Marcin Sendera, Siamak Ravanbakhsh, Gauthier Gidel, Yoshua Bengio, Nikolay Malkin, and Alexander Tong. Iterated Denoising Energy Matching for Sampling from Boltzmann Densities, June 2024. URL <http://arxiv.org/abs/2402.06121>. arXiv:2402.06121 [cs].
- [60] Jiajun He, Yuanqi Du, Francisco Vargas, Dinghuai Zhang, Shreyas Padhy, RuiKang OuYang, Carla Gomes, and José Miguel Hernández-Lobato. No Trick, No Treat: Pursuits and Challenges Towards Simulation-free Training of Neural Samplers, February 2025. URL <http://arxiv.org/abs/2502.06685>. arXiv:2502.06685 [cs].
- [61] W.G. Noid. Systematic Methods for Structurally Consistent Coarse-Grained Models. In Luca Monticelli and Emppu Salonen, editors, *Biomolecular Simulations*, number 924 in Methods in Molecular Biology, pages 487–531. Humana Press, January 2013. ISBN 978-1-62703-016-8. URL http://dx.doi.org/10.1007/978-1-62703-017-5_19.
- [62] Shriram Chennakesavalu, David J. Toomer, and Grant M. Rotskoff. Ensuring thermodynamic consistency with invertible coarse-graining. *The Journal of Chemical Physics*, 158(12):124126, March 2023. ISSN 0021-9606, 1089-7690. doi:10.1063/5.0141888. URL <http://arxiv.org/abs/2210.07882>. arXiv:2210.07882 [cond-mat].
- [63] Grant M. Rotskoff. Sampling thermodynamic ensembles of molecular systems with generative neural networks: Will integrating physics-based models close the generalization gap? *Current Opinion in Solid State and Materials Science*, 30:101158, June 2024. ISSN 1359-0286. doi:10.1016/j.cossms.2024.101158. URL <https://www.sciencedirect.com/science/article/pii/S135902862400024X>.
- [64] Eleftherios Christofi, Petra Bačová, and Vagelis A. Harmandaris. Physics-Informed Deep Learning Approach for Reintroducing Atomic Detail in Coarse-Grained Configurations of Multiple Poly(lactic acid) Stereoisomers. *Journal of Chemical Information and Modeling*, 64(6):1853–1867, March 2024. ISSN 1549-9596. doi:10.1021/acs.jcim.3c01870. URL <https://doi.org/10.1021/acs.jcim.3c01870>. Publisher: American Chemical Society.
- [65] Gerhard Hummer and Ioannis G. Kevrekidis. Coarse Molecular Dynamics of a Peptide Fragment: Free Energy, Kinetics, and Long-Time Dynamics Computations. *The Journal of Chemical Physics*, 118(23):10762–10773, June 2003. ISSN 0021-9606, 1089-7690. doi:10.1063/1.1574777. URL <http://arxiv.org/abs/physics/0212108>. arXiv:physics/0212108.
- [66] Markus Schöberl, Nicholas Zabaras, and Phaedon-Stelios Koutsourelakis. Embedded-physics machine learning for coarse-graining and collective variable discovery without data. *CoRR*, abs/2002.10148, 2020. URL <https://arxiv.org/abs/2002.10148>.
- [67] Patrick G. Sahrman, Timothy D. Loose, Aleksander E. P. Durumeric, and Gregory A. Voth. Utilizing Machine Learning to Greatly Expand the Range and Accuracy of Bottom-Up Coarse-Grained Models through Virtual Particles. *Journal of Chemical Theory and Computation*, February 2023. ISSN 1549-9618. doi:10.1021/acs.jctc.2c01183. URL <https://doi.org/10.1021/acs.jctc.2c01183>. Publisher: American Chemical Society.
- [68] Aapo Hyvärinen. Estimation of Non-Normalized Statistical Models by Score Matching. *Journal of Machine Learning Research*, 6(24):695–709, 2005. ISSN 1533-7928. URL <http://jmlr.org/papers/v6/hyvarinen05a.html>.
- [69] Adji Bousso Dieng, Dustin Tran, Rajesh Ranganath, John Paisley, and David Blei. Variational Inference via χ Upper Bound Minimization. In *Advances in Neural Information Processing Systems*, volume 30. Curran Associates, Inc., 2017. URL <https://proceedings.neurips.cc/paper/2017/hash/35464c848f410e55a13bb9d78e7fddd0-Abstract.html>.

- [70] Diederik P. Kingma and Jimmy Lei Ba. Adam: A method for stochastic optimization. In *3rd International Conference on Learning Representations, ICLR*, dec 2015.
- [71] Christopher M. Bishop. *Pattern Recognition and Machine Learning (Information Science and Statistics)*. Springer, 1 edition, 2007. ISBN 0387310738.
- [72] Rui Shu, Hung H Bui, Shengjia Zhao, Mykel J Kochenderfer, and Stefano Ermon. Amortized inference regularization. In S. Bengio, H. Wallach, H. Larochelle, K. Grauman, N. Cesa-Bianchi, and R. Garnett, editors, *Advances in Neural Information Processing Systems*, volume 31. Curran Associates, Inc., 2018. URL https://proceedings.neurips.cc/paper_files/paper/2018/file/1819932ff5cf474f4f19e7c7024640c2-Paper.pdf.
- [73] Abhinav Agrawal, Daniel R Sheldon, and Justin Domke. Advances in black-box vi: Normalizing flows, importance weighting, and optimization. In H. Larochelle, M. Ranzato, R. Hadsell, M.F. Balcan, and H. Lin, editors, *Advances in Neural Information Processing Systems*, volume 33, pages 17358–17369. Curran Associates, Inc., 2020. URL https://proceedings.neurips.cc/paper_files/paper/2020/file/c91e3483cf4f90057d02aa492d2b25b1-Paper.pdf.
- [74] Tom Minka. Divergence measures and message passing. Technical Report MSR-TR-2005-173, Microsoft Research, January 2005. URL <https://www.microsoft.com/en-us/research/publication/divergence-measures-and-message-passing/>.
- [75] Gohar Ali Siddiqui, Julia A. Stebani, Darren Wragg, Phaeton-Stelios Koutsourelakis, Angela Casini, and Alessio Gagliardi. Application of Machine Learning Algorithms to Metadynamics for the Elucidation of the Binding Modes and Free Energy Landscape of Drug/Target Interactions: a Case Study. *Chemistry – A European Journal*, 29(62):e202302375, 2023. ISSN 1521-3765. doi:10.1002/chem.202302375. URL <https://onlinelibrary.wiley.com/doi/abs/10.1002/chem.202302375>. _eprint: <https://onlinelibrary.wiley.com/doi/pdf/10.1002/chem.202302375>.
- [76] RM Neal. Annealed importance sampling. *STATISTICS AND COMPUTING*, 11(2):125 – 139, 2001. ISSN 0960-3174.
- [77] P. Del Moral, A. Doucet, and A. Jasra. Sequential Monte Carlo samplers. *Journal of the Royal Statistical Society Series B-Statistical Methodology*, 68:411–436, 2006. ISSN 1369-7412. doi:10.1111/j.1467-9868.2006.00553.x.
- [78] Laurent Dinh, Jascha Sohl-Dickstein, and Samy Bengio. Density estimation using real NVP. *CoRR*, abs/1605.08803, 2016. URL <http://arxiv.org/abs/1605.08803>.
- [79] Conor Durkan, Artur Bekasov, Iain Murray, and George Papamakarios. Neural spline flows, 2019. URL <https://arxiv.org/abs/1906.04032>.
- [80] Peter Wirnsberger, Andrew J. Ballard, George Papamakarios, Stuart Abercrombie, Sébastien Racanière, Alexander Pritzel, Danilo Jimenez Rezende, and Charles Blundell. Targeted free energy estimation via learned mappings. *The Journal of Chemical Physics*, 153(14):144112, 10 2020. ISSN 0021-9606. doi:10.1063/5.0018903. URL <https://doi.org/10.1063/5.0018903>.
- [81] Joseph C. Kim, David Bloore, Karan Kapoor, Jun Feng, Ming-Hong Hao, and Mengdi Wang. Scalable normalizing flows enable boltzmann generators for macromolecules, 2024. URL <https://arxiv.org/abs/2401.04246>.
- [82] Taco S. Cohen and Max Welling. Steerable cnns. *CoRR*, abs/1612.08498, 2016. URL <http://arxiv.org/abs/1612.08498>.
- [83] Simon Batzner, Albert Musaelian, Lixin Sun, Mario Geiger, Jonathan P. Mailoa, Mordechai Kornbluth, Nicola Molinari, Tess E. Smidt, and Boris Kozinsky. E(3)-Equivariant Graph Neural Networks for Data-Efficient and Accurate Interatomic Potentials. *Nature Communications*, 13(1):2453, May 2022. ISSN 2041-1723. doi:10.1038/s41467-022-29939-5. URL <http://arxiv.org/abs/2101.03164>. arXiv:2101.03164 [cond-mat, physics:physics].
- [84] Leon Klein, Andreas Krämer, and Frank Noé. Equivariant flow matching, 2023. URL <https://arxiv.org/abs/2306.15030>.
- [85] Daniel Ward. Flowjax: Distributions and normalizing flows in jax, 2024. URL <https://github.com/danielward27/flowjax>.
- [86] Patrick Kidger and Cristian Garcia. Equinox: neural networks in JAX via callable PyTrees and filtered transformations. *Differentiable Programming workshop at Neural Information Processing Systems 2021*, 2021.
- [87] James Bradbury, Roy Frostig, Peter Hawkins, Matthew James Johnson, Chris Leary, Dougal Maclaurin, George Necula, Adam Paszke, Jake VanderPlas, Skye Wanderman-Milne, and Qiao Zhang. JAX: composable transformations of Python+NumPy programs, 2018. URL <http://github.com/jax-ml/jax>.

- [88] Youssef Marzouk, Tarek Moselhy, Matthew Parno, and Alessio Spantini. *Sampling via Measure Transport: An Introduction*, pages 1–41. Springer International Publishing, Cham, 2016. ISBN 978-3-319-11259-6. doi:10.1007/978-3-319-11259-6_23-1. URL https://doi.org/10.1007/978-3-319-11259-6_23-1.
- [89] Matthew D. Parno and Youssef M. Marzouk. Transport map accelerated markov chain monte carlo. *SIAM/ASA Journal on Uncertainty Quantification*, 6(2):645–682, 2018. doi:10.1137/17M1134640. URL <https://doi.org/10.1137/17M1134640>.
- [90] Matthew D. Homan and Andrew Gelman. The no-u-turn sampler: adaptively setting path lengths in hamiltonian monte carlo. *J. Mach. Learn. Res.*, 15(1):1593–1623, January 2014. ISSN 1532-4435.
- [91] Johannes Gasteiger, Janek Groß, and Stephan Günnemann. Directional Message Passing for Molecular Graphs, April 2022. URL <http://arxiv.org/abs/2003.03123>. arXiv:2003.03123 [physics, stat].
- [92] Emil Fischer. Ueber d. und i. Mannozuckersäure. *Berichte der deutschen chemischen Gesellschaft*, 24(1):539–546, 1891. ISSN 1099-0682. doi:10.1002/cber.189102401101. URL <https://onlinelibrary.wiley.com/doi/abs/10.1002/cber.189102401101>. [_eprint: https://onlinelibrary.wiley.com/doi/pdf/10.1002/cber.189102401101](https://onlinelibrary.wiley.com/doi/pdf/10.1002/cber.189102401101).
- [93] Donna G. Blackmond. The Origin of Biological Homochirality. *Cold Spring Harbor Perspectives in Biology*, 11(3):a032540, March 2019. ISSN 1943-0264. doi:10.1101/cshperspect.a032540. URL <https://www.ncbi.nlm.nih.gov/pmc/articles/PMC6396334/>.
- [94] Aaron M. Fluitt and Juan J. de Pablo. An Analysis of Biomolecular Force Fields for Simulations of Polyglutamine in Solution. *Biophysical Journal*, 109(5):1009–1018, September 2015. ISSN 0006-3495, 1542-0086. doi:10.1016/j.bpj.2015.07.018. URL [https://www.cell.com/biophysj/abstract/S0006-3495\(15\)00724-9](https://www.cell.com/biophysj/abstract/S0006-3495(15)00724-9). Publisher: Elsevier.
- [95] Victor Garcia Satorras, Emiel Hoogeboom, Fabian Fuchs, Ingmar Posner, and Max Welling. E(n) equivariant normalizing flows. In M. Ranzato, A. Beygelzimer, Y. Dauphin, P.S. Liang, and J. Wortman Vaughan, editors, *Advances in Neural Information Processing Systems*, volume 34, pages 4181–4192. Curran Associates, Inc., 2021. URL https://proceedings.neurips.cc/paper_files/paper/2021/file/21b5680d80f75a616096f2e791affac6-Paper.pdf.
- [96] Mario Geiger and Tess Smidt. e3nn: Euclidean neural networks, 2022. URL <https://arxiv.org/abs/2207.09453>.
- [97] J.S. Liu. *Monte Carlo Strategies in Scientific Computing*. Springer Series in Statistics. Springer.

Appendices

A Computation of the information-theoretic criterion used for the adaptive tempering scheme

The following note provides a derivation of the information-theoretic criterion used for the adaptive tempering scheme proposed in Section 2.2 and associated computational details.

Based on Equation (9), we can write the numerator and denominator in Equation (22) that provide δKL_k as:

$$KL(q_\theta(\mathbf{X}, \mathbf{z}) || p_\phi(\mathbf{X}, \mathbf{z}; \beta_{k+1})) - KL(q_\theta(\mathbf{X}, \mathbf{z}) || p_\phi(\mathbf{X}, \mathbf{z}; \beta_k)) = \Delta\beta_k \langle U_\phi(\mathbf{X}, \mathbf{z}; \beta) \rangle_{q_\theta(\mathbf{X}, \mathbf{z})} + \log \frac{Z_{\beta_{k+1}}}{Z_{\beta_k}} \quad (31)$$

and

$$KL(q_\theta(\mathbf{X}, \mathbf{z}) || p_\phi(\mathbf{X}, \mathbf{z}; \beta_k)) = \beta_k \langle U_\phi(\mathbf{X}, \mathbf{z}; \beta) \rangle_{q_\theta(\mathbf{X}, \mathbf{z})} + \log Z_{\beta_k} + \langle \log q_\theta(\mathbf{X} | \mathbf{z}) \rangle_{q_\theta(\mathbf{X}, \mathbf{z})} + \langle \log q_\theta(\mathbf{z}) \rangle_{q_\theta(\mathbf{z})} \quad (32)$$

The computation of the terms excluding the partition functions, as discussed in the main text, can be carried out with Monte Carlo or analytically due to the form of q_θ detailed. For the partition function Z_{β_k} and given the proximity of the optimized $q_\theta(\mathbf{X}, \mathbf{z})$ to $p_\phi(\mathbf{X}, \mathbf{z}; \beta_k)$ we employ Importance Sampling (IS) with q_θ as the IS density [97]. In particular:

$$\begin{aligned} \log Z_{\beta_k} &= \log \int e^{-\beta_k U_\phi(\mathbf{X}, \mathbf{z}; \beta)} d\mathbf{X} d\mathbf{z} \\ &= \log \int \frac{e^{-\beta_k U_\phi(\mathbf{X}, \mathbf{z}; \beta_k)}}{q_\theta(\mathbf{X}, \mathbf{z})} q_\theta(\mathbf{X}, \mathbf{z}) d\mathbf{X} d\mathbf{z} \\ &\approx \log \left(\frac{1}{N} \sum_{i=1}^N w^{(i)} \right) \end{aligned} \quad (33)$$

where $w^{(i)}$ denote the *unnormalized* IS weights computed as:

$$w^{(i)} = \frac{e^{-\beta_k U_\phi(\mathbf{X}^{(i)}, \mathbf{z}^{(i)}; \beta_k)}}{q_\theta(\mathbf{X}^{(i)}, \mathbf{z}^{(i)})} \quad (34)$$

where $(\mathbf{X}^{(i)}, \mathbf{z}^{(i)})$ are i.i.d samples drawn from q_θ . To avoid numerical underflow, we operate with the log-weights shifted by their maximum, i.e. $\tilde{w}^{(i)} = \log w^{(i)} - \log w_{max}$ where $\log w_{max} = \max_i \log w^{(i)}$ and use the following estimator:

$$\log Z_{\beta_k} \approx \log \left(\frac{e^{\log w_{max}}}{N} \sum_{i=1}^N e^{\tilde{w}^{(i)}} \right) = \log w_{max} - \log N + \log \left(\sum_{i=1}^N e^{\tilde{w}^{(i)}} \right) \quad (35)$$

Finally, with regard to the $\log \frac{Z_{\beta_{k+1}}}{Z_{\beta_k}}$ term, we have:

$$\begin{aligned} \log Z_{\beta_{k+1}} &= \log \int e^{-\beta_{k+1} U_\phi(\mathbf{X}, \mathbf{z}; \beta_{k+1})} d\mathbf{X} d\mathbf{z} \\ &= \log \int \frac{e^{-(\beta_k + \Delta\beta_k) U_\phi(\mathbf{X}, \mathbf{z}; \beta_{k+1})}}{\frac{e^{-\beta_k U_\phi(\mathbf{X}, \mathbf{z}; \beta_k)}}{Z_{\beta_k}}} \frac{e^{-\beta_k U_\phi(\mathbf{X}, \mathbf{z}; \beta_k)}}{Z_{\beta_k}} d\mathbf{X} d\mathbf{z} \\ &= \log Z_{\beta_k} + \log \int e^{-\Delta\beta_k U_\phi(\mathbf{X}, \mathbf{z})} \frac{e^{-\beta_k U_\phi(\mathbf{X}, \mathbf{z}; \beta_k)}}{q_\theta(\mathbf{X}, \mathbf{z})} \frac{q_\theta(\mathbf{X}, \mathbf{z})}{Z_{\beta_k}} d\mathbf{X} d\mathbf{z}. \end{aligned} \quad (36)$$

(from Equation (5))

Hence:

$$\begin{aligned}
 \log \frac{Z_{\beta_{k+1}}}{Z_{\beta_k}} &= \log \int e^{-\Delta\beta_k U(\mathbf{f}_\phi(\mathbf{X}, \mathbf{z}))} w(\mathbf{X}, \mathbf{z}) \frac{q_\theta(\mathbf{X}, \mathbf{z})}{Z_{\beta_k}} d\mathbf{X} d\mathbf{z} \\
 &\approx \log \left(\frac{1}{N} \sum_{i=1}^N e^{-\Delta\beta_k U(\mathbf{f}_\phi(\mathbf{X}^{(i)}, \mathbf{z}^{(i)}))} \frac{w^{(i)}}{Z_{\beta_k}} \right) \\
 &= \log \left(\sum_{i=1}^N e^{-\Delta\beta_k U(\mathbf{f}_\phi(\mathbf{X}^{(i)}, \mathbf{z}^{(i)}))} W^{(i)} \right) \tag{37}
 \end{aligned}$$

where $W^{(i)} = \frac{w^{(i)}}{\sum_{j=1}^N w^{(j)}}$ are the *normalized* IS weights. As before, we can employ the shift of the log-weights to avoid numerical underflow problems in the computation of $W^{(i)}$.